US Army Corps
of Engineers®
Engineer Research and
Development Center

20040329 081

Probability Distributions for the Refractive Index Structure Parameter and the Inner Scale of Turbulence and Their Implications for Flux Averaging

Edgar L Andreas, Christopher W. Fairall, P. Ola G. Persson, and Peter S. Guest

December 2003

Cold Regions Research and Engineering Laboratory
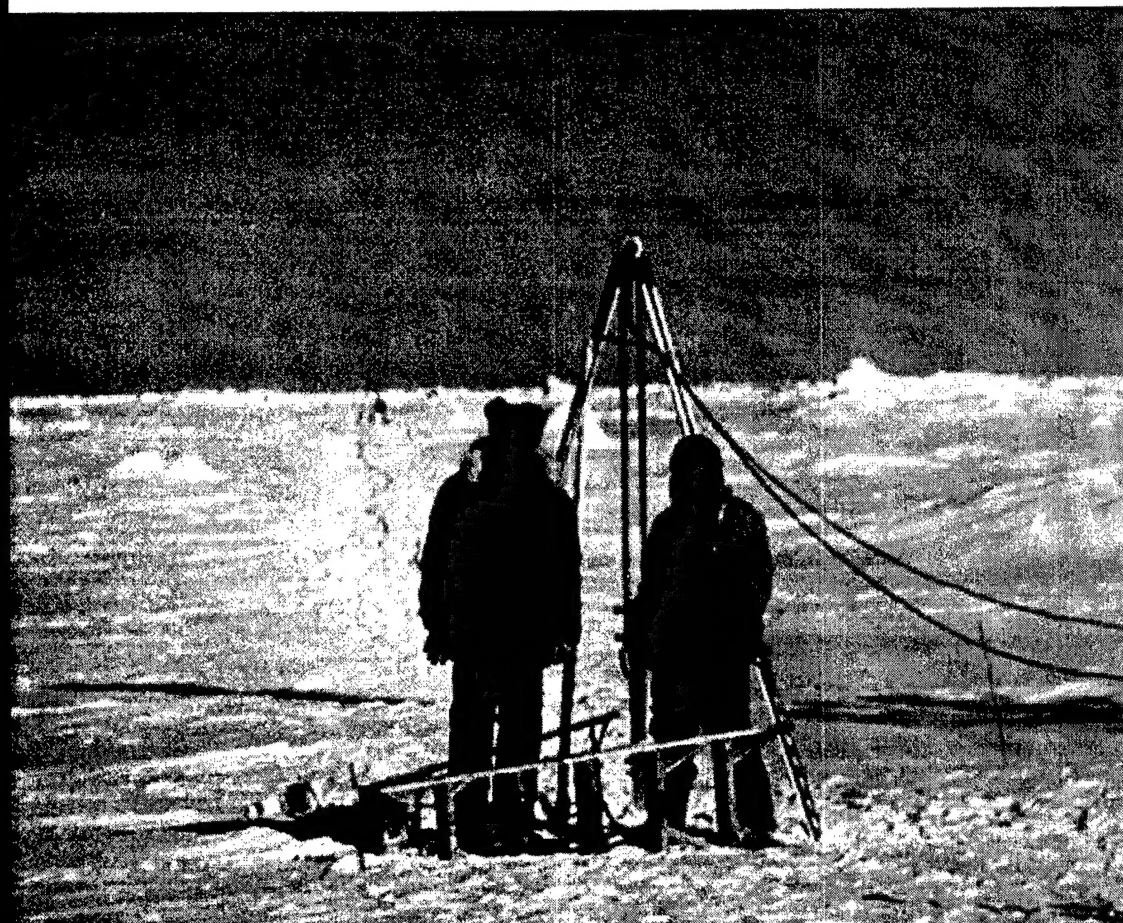
Front Cover: Dave Costa and Ed Andreas pose at the receiver of the scintillometer at the SHEBA ice camp in May 1998. The scintillometer transmitter is 300 m in the distance.

ABSTRACT

Defining the averaging time required for measuring meaningful turbulence statistics is a central problem in boundary-layer meteorology. Path-averaging scintillation instruments are presumed to confer some time-averaging benefits when the objective is to measure surface fluxes, but that hypothesis has not been tested definitively. This study uses scintillometer measurements of the inner scale of turbulence (ℓ_0) and the refractive index structure parameter (C_n^2) collected during SHEBA (the experiment to study the Surface Heat Budget of the Arctic Ocean) to investigate this question of required averaging time. The first conclusion is that the beta probability distribution is useful for representing C_n^2 and ℓ_0 measurements. Consequently, beta distributions are used to set confidence limits on C_n^2 and ℓ_0 values obtained over various averaging periods. When the C_n^2 and ℓ_0 time series are stationary, a short-term average of C_n^2 or ℓ_0 can be as accurate as a long-term average. But, as with point measurements, when time series of path-averaged C_n^2 or ℓ_0 values are nonstationary, turbulent surface fluxes inferred from these C_n^2 and ℓ_0 values can be variable and uncertain—problems that path-averaging was presumed to mitigate. Since nonstationarity turns out to be a limiting condition, the last topic is quantifying the nonstationarity with a published nonstationarity ratio and also by simply counting zero-crossings in the time series.

CONTENTS

ILLUSTRATIONS

TABLE

PREFACE

Probability Distributions for the Refractive Index Structure Parameter and the Inner Scale of Turbulence and Their Implications for Flux Averaging

EDGAR L ANDREAS, CHRISTOPHER W. FAIRALL,
P. OLA G. PERSSON, AND PETER S. GUEST

1   INTRODUCTION

The wide-ranging fields of atmospheric optics and boundary-layer meteorology intersect when the subject is optical turbulence. The classic works by Tatarskii (1961, 1971) and Chernov (1967) define the scope of this intersection. More recently, Andreas (1990) assembled classic papers from both disciplines that focus on obtaining turbulent fluxes in the atmospheric boundary layer from the propagation statistics obtained at optical or other electromagnetic (EM) wavelengths.

This idea of using the propagation statistics of EM waves—especially those that quantify scintillation—to infer turbulent properties of the atmospheric boundary layer has been around for about 35 years (e.g., Strohbehn 1970, Gray and Waterman 1970, Gurvich et al. 1974). Because of the need to evaluate the surface energy budget over terrain that may be inhomogeneous, the emphasis in the last 20 years has been on using scintillation statistics to infer the surface fluxes of heat, moisture, and momentum (e.g., Kohsiek and Herben 1983, Hill et al. 1988, 1992a, 1992b, Andreas 1989b, 1992, Thiermann and Grassl 1992, Green et al. 1994, De Bruin et al. 1995, Nieveen and Green 1999).

Two propagation statistics are commonly used to estimate turbulent fluxes in the atmospheric surface layer: the refractive index structure parameter, C_n^2, and the inner scale of turbulence, ℓ_0. The refractive index structure parameter sets the level of the inertial-convective subrange for the one-dimensional refractive index spectrum, Φ_n (e.g., Andreas 1987):

$$\Phi_n(\kappa) = 0.249 C_n^2 \kappa^{-5/3} , \qquad\qquad (1.1)$$

where κ is the magnitude of the turbulence wavenumber. The refractive index spectrum in the inertial-convective subrange, however, can also be expressed in more familiar meteorological variables:

$$\Phi_n(\kappa) = \beta_n N_n \varepsilon^{-1/3} \kappa^{-5/3} , \tag{1.2}$$

where N_n is the dissipation rate of the variance in refractive index, ε is the dissipation rate of turbulence kinetic energy, and β_n (~ 0.4, Andreas 1987) is the Kolmogorov (or Corrsin) constant for the refractive index spectrum.

For the optical wavelengths that we use, C_n^2 relates directly to the temperature structure parameter C_T^2 through

$$C_n^2 = A^2(\lambda, P, T, Q) C_T^2 . \tag{1.3}$$

Here, A is a known function of the EM wavelength (λ) and the average barometric pressure (P), temperature (T), and specific humidity (Q) (e.g., Andreas 1988b).

In (1.3), we ignore contributions from the humidity and temperature-humidity structure parameters. These contributions are usually negligible unless the absolute value of the Bowen ratio is small (e.g., Wesely and Alcarez 1973, Wesely 1976, Thiermann and Grassl 1992, Hill et al. 1992b). Over sea ice, the magnitude of the Bowen ratio is almost always large enough for (1.3) to be a good approximation (Andreas and Cash 1996).

Because the temperature spectrum also obeys equations like (1.1) and (1.2), (1.3) can be written as

$$C_n^2 = A^2(\beta_T / 0.249) N_T \varepsilon^{-1/3} , \tag{1.4}$$

where β_T is the Kolmogorov constant for the temperature spectrum, and N_T is the dissipation rate of temperature variance. As a result, C_n^2 is related to dissipation rates that are commonly used in the so-called inertial-dissipation method for flux estimation (e.g., Fairall and Larsen 1986).

The inner scale of turbulence ℓ_0 likewise relates to features of the refractive index spectrum; ℓ_0 is approximately the turbulent eddy size that separates the inertial-convective subrange from the dissipation region and is roughly seven times larger than the Kolmogorov microscale. Because at optical wavelengths

the temperature spectrum and the refractive index spectrum have identical shapes at large wavenumbers, we can write (Hill and Clifford 1978)

$$\ell_0 = \left[9\Gamma(1/3)\beta_T D\right]^{3/4} \varepsilon^{-1/4} , \tag{1.5}$$

where Γ is the gamma function and D is the thermal diffusivity of air. Like C_n^2, the propagation statistic ℓ_0 is related to a dissipation value (i.e., ε) that is required for using the inertial-dissipation method to estimate the turbulent surface stress.

Two routes are available now for estimating the surface stress (or momentum flux) and the sensible heat flux from these scintillation measurements. One way is to use the dissipation rates ε and N_T computed from (1.5) and (1.4), respectively, in the traditional inertial-dissipation equations (e.g., Large and Pond 1982, Fairall and Larsen 1986, Edson et al. 1991). The second way is to use the measured refractive index structure parameter in a similarity relation for the temperature structure parameter.

For this latter method, the two relevant equations are (e.g., Andreas 1988b, Thiermann and Grassl 1992, Hill 1997)

$$t_* = \left[\frac{z^{2/3} C_n^2}{A^2 g(\zeta)}\right]^{1/2} \tag{1.6}$$

and

$$u_* = \left[\frac{\varepsilon k z}{\phi_\varepsilon(\zeta)}\right]^{1/3} . \tag{1.7}$$

Here, z is the path height, k is the von Kármán constant, and $g(\zeta)$ and $\phi_\varepsilon(\zeta)$ are semi-empirical Monin–Obukhov similarity functions of the stability parameter $\zeta = z/L$, where L is the Obukhov length (see Appendix A). Also in these, u_* is the friction velocity and t_* is a temperature flux scale such that $\tau = \rho u_*^2$ is the surface stress and $H_s = -\rho c_p u_* t_*$ is the surface sensible heat flux, where ρ is the air density and c_p is the specific heat of air at constant pressure. Note that, because of the square root, (1.6) is ambiguous as to the sign of t_*; we must evaluate this by other means.

Using scintillation statistics to estimate the turbulent surface fluxes is attractive because the EM waves propagate over some finite path. The propagation statistics are thus path-averaged, as would be any turbulence quantity derived from them. Presumably, such path-averaging would mitigate the effects of minor nonstationarity or surface heterogeneity that often confound turbulence measurements made with point sensors (Schmid and Oke 1990, Horst and Weil 1992, 1994).

A second supposed benefit of using EM propagation measurements of C_n^2 and ℓ_0 to determine u_* and t_* is that statistically reliable values of C_n^2 and ℓ_0 can be obtained with very short averaging times, on the order of one minute or less (Wyngaard and Clifford 1978, Frehlich 1988). By extension, this result would seem to suggest that τ and H_s could also be measured using path-averaging instruments with much shorter averaging times than the 30–60 minutes of averaging typically required for point measurements (Haugen et al. 1971, Wyngaard 1973, Sreenivasan et al. 1978).

The rationale for this idea that short flux-averaging times are possible is that a path-averaging sensor samples many more turbulent eddies per unit time than a point sensor (Andreas 1988a). Some of those eddies would, presumably, be the larger ones that manifest as nonstationarity or intermittency in a time series of point measurements. The path-averaging supposedly would smooth out the effects of these large eddies and thereby reduce the sampling error common in point measurements of turbulent fluxes.

Even if this scenario is accurate, though, we are still skeptical that path-averaged scintillation statistics can routinely yield meaningful estimates of τ and H_s for averaging times on the order of minutes. Obtaining these turbulent flux estimates requires convolving the scintillation statistics C_n^2 and ℓ_0 (or, equivalently, ε) iteratively with the Monin–Obukhov similarity functions $g(\zeta)$ and $\phi_\varepsilon(\zeta)$ in (1.6) and (1.7). All evaluations of these similarity functions that we know of, however, are based on point measurements of mean meteorological and turbulence quantities averaged for 30–60 minutes (e.g., Businger et al. 1971, Dyer and Bradley 1982, Högström 1988, Oncley et al. 1996, Edson and Fairall 1998). It is not obvious to us that, in general, combining minute averages of C_n^2 and ℓ_0 with functions based on at least 30-minute averages yields meaningful values of τ and H_s (cf. Andreas 1988a). If short-term averages of C_n^2 and ℓ_0 are representative of time series averaged for, say, 30–60 minutes, however, using these short-term averages in (1.6) and (1.7) to estimate τ and H_s may be defensible.

Here we address these issues of how to properly average scintillation-derived values of C_n^2 and ℓ_0 for the purpose of estimating the turbulent surface fluxes.

First we review the time-averaging constraints for evaluating Monin–Obukhov similarity functions to highlight our concern over combining similarity functions with short-term scintillometer averages. Next we show seasonal histograms for C_n^2 and ℓ_0 values based on 600 hours of scintillometer data collected during SHEBA, the experiment to study the Surface Heat Budget of the Arctic Ocean. We find that beta probability distributions fit both variables well. We also show that beta distributions fit hour-long series of C_n^2 and ℓ_0 values that contain only 60 points. We therefore use beta distributions to compute error bars for several representative hour-long time series of SHEBA C_n^2 and ℓ_0 values. This error analysis reveals that intermittency and nonstationarity can have pronounced effects on these path-averaged C_n^2 and ℓ_0 values, contrary to some of our earlier speculation. As a result, we reiterate that short-term averages of C_n^2 and ℓ_0 can yield reliable short-term averages of τ and H_s only for quasi-stationary time series.

2   OBSERVATIONS

SHEBA was a multidisciplinary, yearlong experiment on drifting sea ice in the Beaufort Gyre (Perovich et al. 1999, Uttal et al. 2002). Andreas et al. (1999) and Persson et al. (2002) describe our SHEBA program. Andreas et al. (2000) make a preliminary report of our current analysis, and Andreas et al. (2003) give a shorter version of this report.

Our SHEBA scintillometer (Fig. 1) was an SLS20 system made by Scintec Atmosphärenmesstechnik GmbH of Tübingen, Germany (Thiermann 1992). Its source is a laser of 0.685-μm wavelength. We operated this system over a 350-m path at a height of 2.88 m for our 1997 SHEBA measurements and over a 300-m path at a height of 2.60 m for our 1998 measurements. The surface was generally snow-covered sea ice.
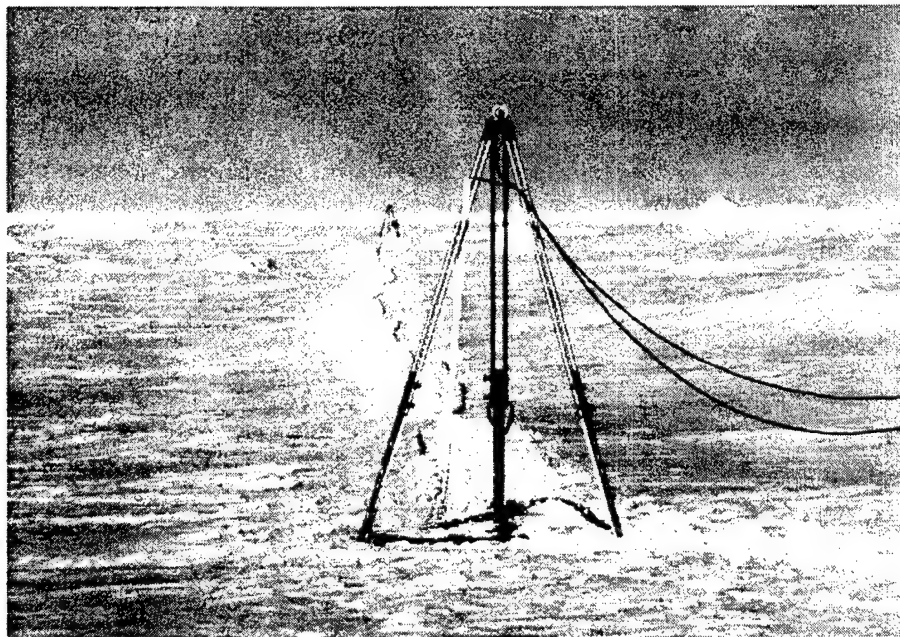

Figure 1. The scintillometer receiver at the SHEBA ice camp. The scintillometer transmitter is in the distance.

At the scintillometer source, the laser beam is split into two beams with their centers separated by 2.7 mm. The scintillometer receiver thus has two detectors, also separated by 2.7 mm. The correlation between the intensity fluctuations at

the two detectors is a measure of ℓ_0. The intensity fluctuations measured by either detector are related to C_n^2.

The fundamental data that the SLS20 reports are minute averages of C_n^2 and ℓ_0 and a data-quality number designated NOK (for number okay). To obtain these averages and NOK, the system software divides each minute into ten 6-s blocks. During the first block of each minute, the software turns the laser off, and the receiver measures the background. The system software then applies this background calibration to the nine subsequent 6-s blocks in that minute. Each of these nine blocks yields an individual measurement of C_n^2 and ℓ_0; the software also evaluates the quality of each 6-s block. If a block passes the quality-control criteria, its C_n^2 and ℓ_0 values are used for computing the minute average; otherwise, that block's values are ignored. NOK reports how many of the nine available data blocks during the minute were used to compute the minute averages of C_n^2 and ℓ_0. To compile the histograms that we show in Section 4, we rejected any minute-averaged C_n^2 and ℓ_0 values that were not based on at least three valid 6-s blocks during that minute. That is, we retained the minute-averaged C_n^2 and ℓ_0 values for further analysis only if NOK, which is reported as a percentage, was at least 33% [= (3/9)×100%].

Figure 2 shows a daylong time series of typical minute-averaged C_n^2 and ℓ_0 values. Generally, ℓ_0 is inversely related to the wind speed; higher wind speeds increase the dissipation rate of turbulent kinetic energy, which, in turn, is associated with smaller ℓ_0 values [see (1.5)]. The behavior of C_n^2 is not as easy to understand. On the one hand, higher wind speeds usually foster mixing, which erodes any vertical temperature gradient, so C_n^2 decreases (cf. Frederickson et al. 2000). But on the other hand, if some process such as radiative heating or cooling can maintain a vertical temperature gradient, a higher wind speed would increase the magnitude of the sensible heat flux and, thereby, increase C_n^2.

Later we will compute statistics from series of C_n^2 and ℓ_0 such as in Figure 2 and derive confidence limits from these statistics. Such analyses get complicated if adjacent samples in the time series are correlated. The autocorrelation function is typically used to quantify the decorrelation time of a random process. The integral of the autocorrelation function over all time lags defines a time $\mathfrak{I}$ called the integral scale (e.g., Lumley and Panofsky 1964, p. 36f.) that quantifies this decorrelation time. Sample values separated in time by intervals of $\mathfrak{I}$ or longer are essentially uncorrelated or independent.

As an estimate for the integral scale in the neutrally stratified atmospheric surface layer, Wyngaard (1973) used

$$\Im \sim \frac{z}{U} , \tag{2.1}$$

where z is again the measurement height and U is the average wind speed at height z. Edson et al. (1991) refined this estimate a little and suggested

$$\Im \simeq \frac{2z}{U_{10}} , \tag{2.2}$$

where U_{10} is the average wind speed at a height of 10 m.
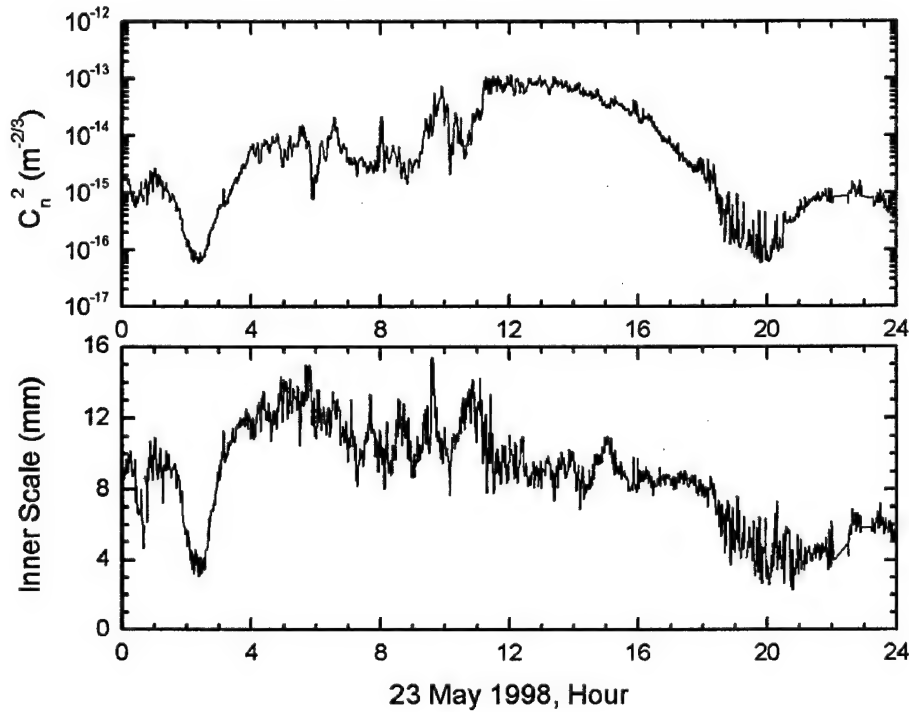
Figure 2. A day of minute-averaged inner scale (ℓ_0) and refractive index structure parameter (C_n^2) values at a height of 3 m from SHEBA.

From high-frequency time series of temperature, humidity, and velocity components, Sreenivasan et al. (1978) actually computed autocorrelation and cross-correlation functions. From the autocorrelation functions for the individual variables, they deduced

$$\mathfrak{I} \simeq \frac{4z}{U}.$$ (2.3)

Their analysis of the cross-correlations, on the other hand, yielded a multiplicative constant in (2.3) that was typically 1.2.

To be conservative, we will use (2.3) to estimate the integral scale. Before considering our scintillometer data, though, we can confirm the usefulness of (2.3) with computations reported by Treviño and Andreas (2000). For three short records of the longitudinal velocity component from a sonic anemometer sampling at 10 Hz, they evaluated a quantity they called the "memory," which approximates the decorrelation time or $\mathfrak{I}$. These memory values ranged from 0.88 to 1.46 s. For their measurements, z was 4 m and U was about 2 m s^{-1}. Equation (2.3) thus predicts $\mathfrak{I} = 8$ s for these data, which is a conservative estimate of the computed decorrelation times.

Our scintillometer operated at heights a bit under 3 m; in (2.3), we will thus use 3 m for z. The integral scale clearly increases as the wind speed decreases; hence, the largest estimate of the decorrelation time is associated with the lightest winds. In fewer than 10 of the 600 hours of scintillometer data that survived our quality controls was the average hourly wind speed less than 1 m s^{-1}. Substituting 1 m s^{-1} and z = 3 m in (2.3) gives 12 s as a conservative estimate for the decorrelation time of our raw scintillometer data. For most of the data, the decorrelation time is much shorter because the wind speed was higher. Since the only scintillometer data we use in our subsequent analyses are minute averages, we can be confident that these minute-averaged C_n^2 and ℓ_0 values are independent. We thus need not worry about the complicating effects of correlated data in our statistical analysis.

3   AVERAGING TO ESTABLISH MONIN–OBUKHOV SIMILARITY THEORY

Equations (1.6) and (1.7), which are needed to convert scintillometer measurements to flux estimates, derive from Monin–Obukhov similarity theory. Evaluating the similarity functions $g(\zeta)$ and $\phi_\varepsilon(\zeta)$ that make (1.6) and (1.7) work requires measuring both means and covariances. In particular, we must measure the mean wind speed (U) and temperature (T) profiles and the covariances $\overline{uw}$ $(=-u_*^2)$ and $\overline{wt}$ $(=-u_* t_*)$, where the overbar denotes averaging. To have confidence in the resulting similarity functions, we must have confidence in the statistical properties of these averages. That is, we must average long enough to ensure reliable statistics.

Lumley and Panofsky (1964, p. 35ff.), Wyngaard (1973), Sreenivasan et al. (1978), Andreas (1988a), and Lenschow et al. (1994), among others, estimate how low is long enough to average. Here we rely on the analyses by Wyngaard and Sreenivasan et al.

Building on work by Lumley and Panofsky (1964), Wyngaard (1973) estimated the averaging time T_x required to reduce the error in a measured mean $\overline{x}$ to $\delta_x \overline{x}$. He obtained

$$T_x = 2\Im_x \frac{\overline{x^2}}{\delta_x^2 \overline{x}^2} ,$$ (3.1)

where $\Im_x$ denotes the integral scale of variable x, and $\overline{x^2}$ is the ensemble variance about $\overline{x}$. As we mentioned earlier, Sreenivasan et al. (1978) evaluated $\Im$ for quantities like U, T, $\overline{uw}$, and $\overline{wt}$. In general, they found

$$\Im_x = \frac{\alpha_x z}{U} ,$$ (3.2)

where α_x is 3.9, 4.9, 1.2, and 1.2 for U, T, $\overline{uw}$, and $\overline{wt}$, respectively.

Evaluating the Monin–Obukhov similarity functions requires measuring the vertical gradients in wind speed and potential temperature. We must, thus, require an accuracy in individual wind speed and temperature measurements of, say, 5 cm s^{-1} and 0.1 K, respectively. For a 5-m s^{-1} wind speed, this makes $\delta_U = 0.01$; for an average temperature of 293 K, $\delta_T = 0.00034$.

To estimate the averaging time for finding the vertical gradient in wind speed, combine (3.1) and (3.2) to get

$$T_U = 2 \times 10^4 \left(\frac{3.9z}{U} \right) \left(\frac{\sigma_U^2}{U^2} \right), \tag{3.3}$$

where σ_U^2 is the variance in the longitudinal component of the wind vector. Typically, $\sigma_U/U \approx 0.1$ (e.g., Arya 1988). Hence, for a 10-m profiling tower in a 5-m s^{-1} wind, $T_U \approx 1600$ s ≈ 26 minutes is an approximate averaging time.

Similarly, to measure the mean vertical temperature gradient, we must average according to

$$T_T = 1.7 \times 10^7 \left(\frac{4.9z}{U} \right) \left(\frac{\sigma_T^2}{T^2} \right). \tag{3.4}$$

When the sensible heat flux is on the order of 100 W m^{-2}, σ_T^2 is about 0.5 K^2. Hence, for an average temperature of 293 K and the other conditions as above, $T_T \approx 970$ s ≈ 16 minutes is an approximate averaging time.

That is, measuring the mean profiles necessary to determine the Monin–Obukhov similarity functions requires averaging for 15 to 30 minutes.

To estimate the flux-averaging time, Wyngaard (1973) and Sreenivasan et al. (1978) wrote (3.1) as

$$T_{wx} = \frac{2\alpha_{wx} z}{\delta_{wx}^2 U} \left[\frac{\overline{(wx)^2} - \overline{wx}^2}{\overline{wx}^2} \right], \tag{3.5}$$

where x is now the turbulent fluctuation in either the longitudinal velocity (u) or temperature (t). From Kansas data, Wyngaard estimated the bracketed quantity in (3.5) to be about 10 for both $\overline{uw}$ and $\overline{wt}$ for near-neutral stratification. Sreenivasan et al. report that this quantity is 15 and 32, respectively, for $\overline{uw}$ and $\overline{wt}$.

An error of 10% (i.e., $\delta_{wx} = 0.1$) is about the best that has been demonstrated for eddy-correlation measurements of the turbulent surface fluxes. Thus, for a measurement height of 5 m, a mean wind speed of 5 m s^{-1}, and with $\alpha_{wx} = 1.2$ from Sreenivasan et al. (1978) for both $\overline{uw}$ and $\overline{wt}$, (3.5) gives $T_{uw} = T_{wt} \approx 40$ minutes when we use Wyngaard's (1973) value for the bracketed term in (3.5).

When we use the estimates for this term from Sreenivasan et al., $T_{uw} \approx 60$ minutes and $T_{wt} \approx 128$ minutes.

In summary, using eddy correlation to measure the momentum and heat fluxes to within 10% for evaluating the Monin–Obukhov similarity functions requires roughly an hour of averaging. (Admittedly, we have ignored stratification effects on these estimates for simplicity and because these effects are not well known for the required covariance statistics.) We could, of course, average the fluxes over shorter intervals to match the averaging time of about 15 minutes we estimated for the wind speed and temperature gradients. But the error in the fluxes would increase with shorter averaging. From (3.5) we can estimate by how much. For example, reducing the averaging time from one hour to 15 minutes would increase the flux error by a factor of 2—from 10% to 20% in our analysis.

We have undertaken this discussion to establish the averaging constraints under which typical Monin–Obukhov similarity functions must be evaluated. Statistical theory and experiment suggest that it may be possible to evaluate these functions from only 15 minutes of averaging, but the results will be quite scattered (cf. Haugen et al. 1971, Wyngaard 1973, p. 141), especially since ζ includes both u_* and t_* and their uncertainties add [see (A3)]. In fact, we know of no attempts to validate Monin–Obukhov similarity theory with such short averages. Almost all published similarity functions are based on averages of 30–60 minutes.

The hope is that scintillometer measurements, because of their path-averaging, might provide relief from these averaging constraints. But the reality is that computing surface fluxes from scintillation measurements requires using similarity functions derived from long averaging times. No evidence exists that Monin–Obukhov similarity theory is also valid for the 1–10 minute fluxes often computed from scintillation data (e.g., Thiermann and Grassl 1992, De Bruin et al. 2002, Hartogensis et al. 2002). To us, assuming that Monin–Obukhov similarity functions derived from 30–60 minute averages are equally valid when applied to short averages is unjustified.

If, however, the path-averaging in scintillation measurements provides such a large, fast sample that, say, 10 minutes of averaging provides the same information that 30–60 minutes of averaging would, using existing Monin–Obukhov similarity functions for computing scintillometer-derived fluxes may be justified. In this paper, we thus study whether short-term samples of scintillometer C_n^2 and ℓ_0 values faithfully represent the behavior of these quantities over an hour. If the answer is "yes" in general, using short scintillometer averages and the Monin–Obukhov similarity functions to compute short-term fluxes is defensible because the path-averaging has mitigated the time-averaging constraints that hamper point

measurements. If the answer is "no," however, scintillometers confer no time-averaging benefits because their data must still pass through the traditional Monin–Obukhov similarity functions to yield surface fluxes.

4 C_n^2 AND ℓ_0 DISTRIBUTIONS

To fairly compare the 1997 and 1998 data sets, we extrapolated both the C_n^2 and ℓ_0 values to a reference height of 3 m on the basis of (1.5), (1.6), and (1.7). That is,

$$C_n^2(3) = C_n^2(z)\left(\frac{z}{3.00}\right)^{2/3} \qquad (4.1)$$

and

$$\ell_0(3) = \ell_0(z)\left(\frac{3.00}{z}\right)^{1/4}, \qquad (4.2)$$

where $C_n^2(z)$ and $\ell_0(z)$ are the values measured at path height z, and $C_n^2(3)$ and $\ell_0(3)$ are the extrapolated values at 3 m. Clearly, (4.1) and (4.2) ignore the stability dependencies contained in $g(\zeta)$ and $\phi_\epsilon(\zeta)$. But since the extrapolations are, at most, just 40 cm, we are safe with the approximations that $g(3/L)/g(z/L)$ and $[\phi_\epsilon(3/L)/\phi_\epsilon(z/L)]^{1/4}$ are both near 1.

Of the 600 hours of scintillometer data that survived our quality controls, almost all of the data collected in unstable stratification had z/L values between −1 and 0, with the majority between −0.1 and 0. The data collected in stable stratification featured z/L values as large as 10, but most z/L values were between 0 and 2.

On using measurements of u_* and H_s from another Arctic experiment, AIDJEX (the Arctic Ice Dynamics Joint Experiment), Andreas (1989a) inferred C_n^2 from a relation similar to (1.6) and found that a beta distribution fitted seasonal histograms of these values well. Figures 3–6 show similar seasonal histogram of our SHEBA C_n^2 and ℓ_0 measurements for autumn (namely, October and November 1997), winter (namely, December 1997), spring (namely, May 1998), and summer (June, July, and August 1998).

Briefly, the beta probability distribution function of random variable y is (e.g., Harr 1987, p. 79 ff.)

$$p(y) = \frac{1}{(b-a)\,\beta(m+1,n+1)}\left(\frac{y-a}{b-a}\right)^m\left(\frac{b-y}{b-a}\right)^n. \qquad (4.3)$$

Here a and b are, respectively, the lower and upper bounds on y; β is the beta function (Abramowitz and Stegun 1965, p. 258),

$$\beta(m+1, n+1) = \frac{\Gamma(m+1)\Gamma(n+1)}{\Gamma(m+n+2)} \; ; \tag{4.4}$$

and Γ is, again, the gamma function (Abramowitz and Stegun 1965, p. 255).

On calculating the sample mean ($\overline{y}$) and sample standard deviation (s_y) of y, we define two new variables

$$\hat{y} = (\overline{y} - a)/(b - a) \tag{4.5}$$

and

$$\hat{V} = \left[s_y/(b-a) \right]^2 . \tag{4.6}$$

These then predict the parameters m and n:

$$m = (\hat{y}^2/\hat{V})(1 - \hat{y}) - (1 + \hat{y}) , \tag{4.7}$$

$$n = (m+1)/\hat{y} - (m+2) . \tag{4.8}$$

In Figures 3–6, since we plotted C_n^2 on a logarithmic scale, we also based our fitted histograms on the logarithm of C_n^2. That is, in calculating the sample mean and sample standard deviation and in setting the a and b values in the beta distributions for the seasonal C_n^2 histograms, we used $\ln\left(C_n^2\right)$ rather than C_n^2.

Because of instrument problems and the resulting sparse data returns in some seasons, our seasonal C_n^2 histograms in Figures 3–6 are not as representative of the true Arctic seasons as Andreas's (1989a). Rather, we offer the C_n^2 histograms in Figures 3–6 as further evidence that the beta distribution is useful for representing the variability in this statistic. The ℓ_0 histograms in Figures 3–6 are, we believe, the first attempts at constructing seasonal histograms for ℓ_0.
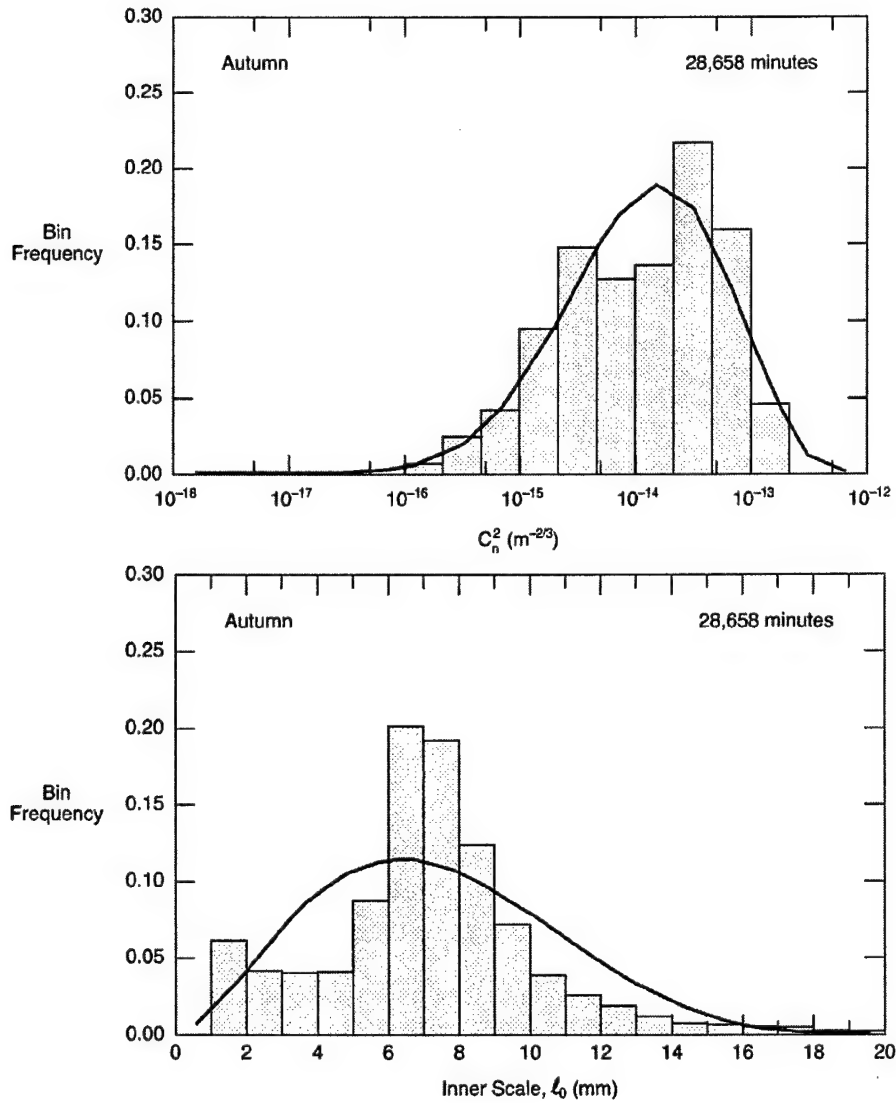
Figure 3. Histograms of the minute-averaged C_n^2 and ℓ_0 values measured at SHEBA during autumn (namely, October and November 1997). The number in the upper right corner gives the number of minute-averaged values used to create the histogram. The solid curve is a beta distribution fitted to the histogram. In the C_n^2 plot, the lower and upper limits of the beta distribution, a and b, are $\ln\left(10^{-18}\,\text{m}^{-2/3}\right)$ and $\ln\left(10^{-12}\,\text{m}^{-2/3}\right)$, respectively; in the ℓ_0 plot, these limits are 0 and 20 mm.
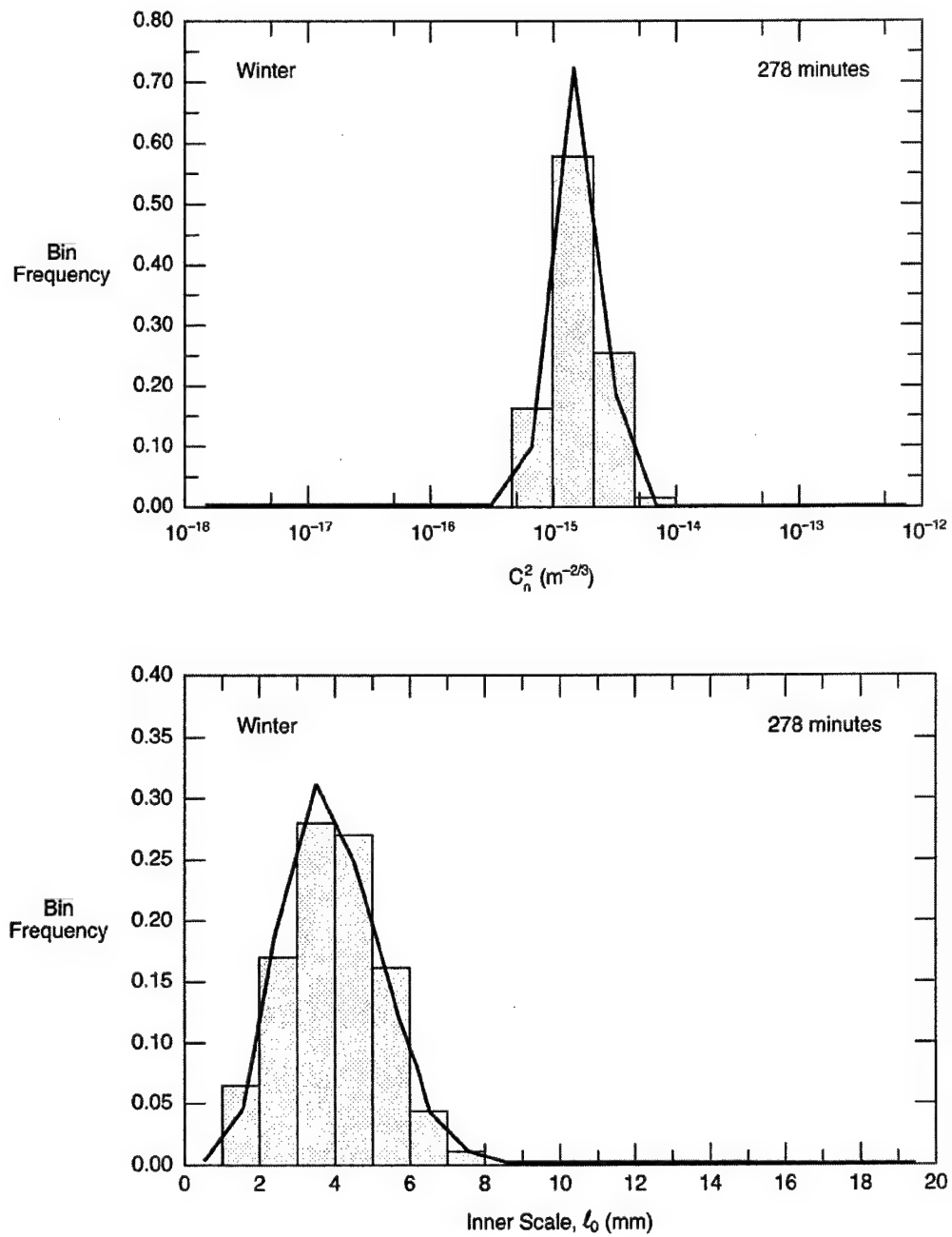
Figure 4. As in Figure 3 except for winter (that is, December 1997).
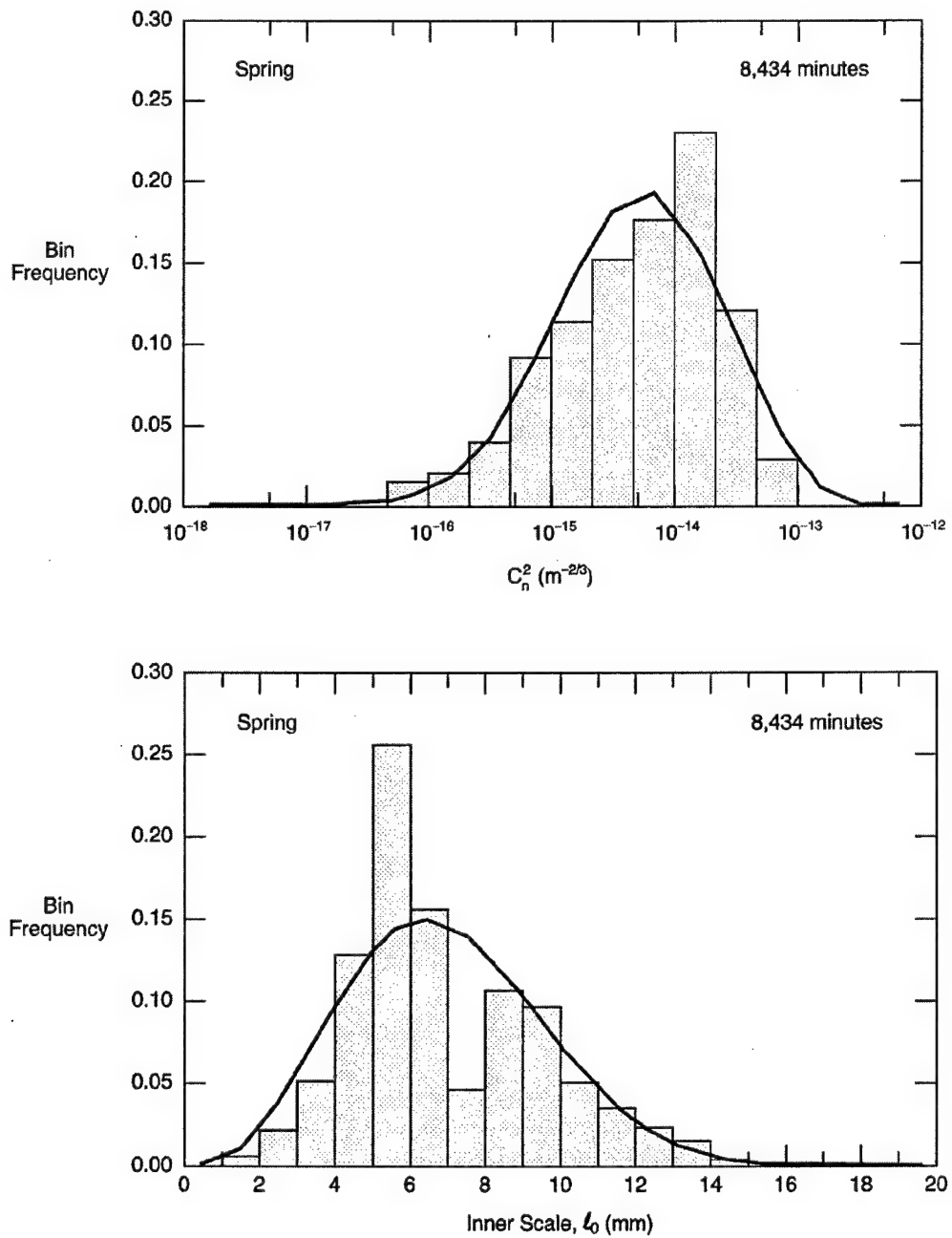
Figure 5. As in Figure 3 except for spring (that is, May 1998).
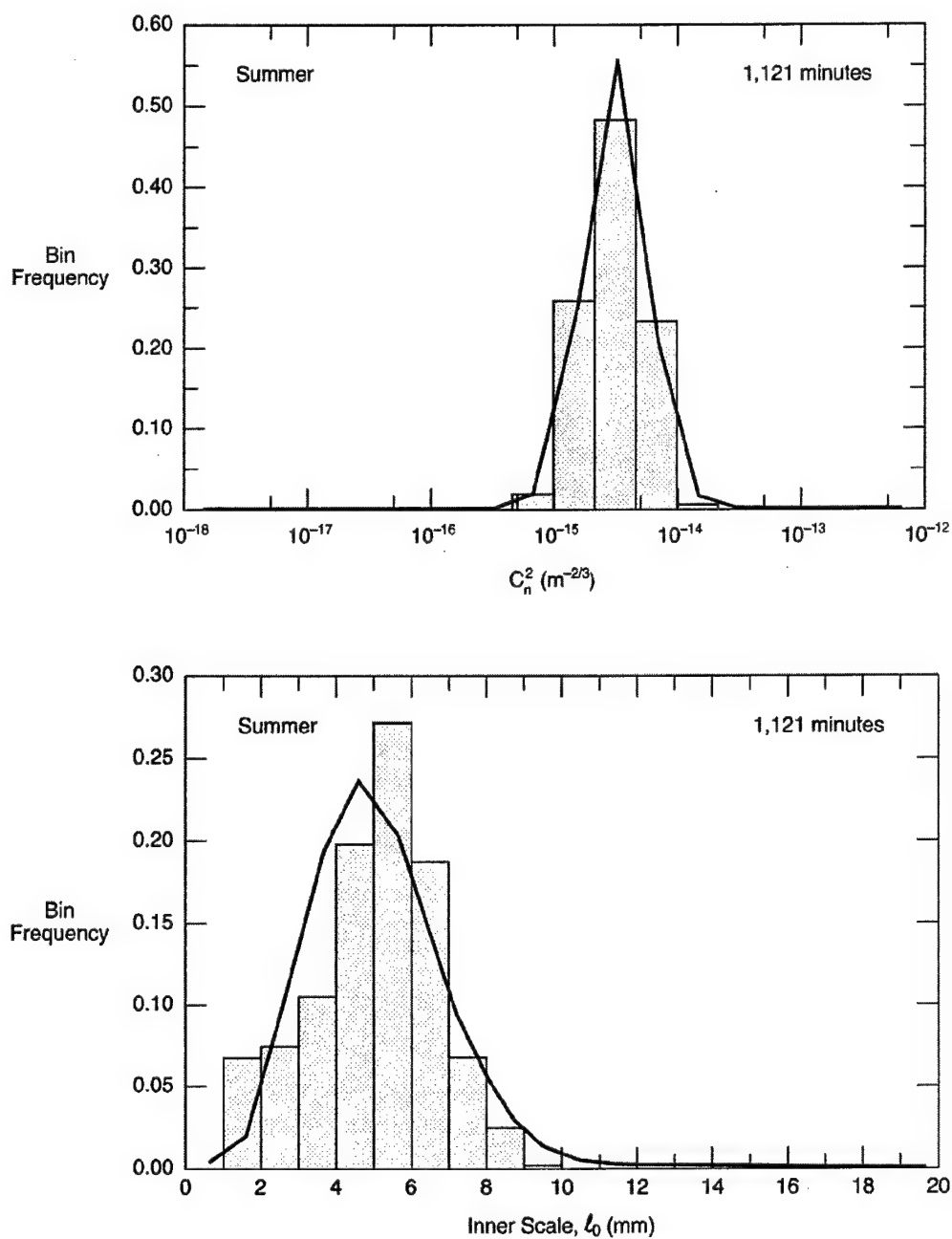
Figure 6. As in Figure 3 except for summer (June, July, August 1998).

Although the beta distribution requires four parameters (i.e., $\bar{y}$, s_y, a, b), rather than the two needed for normal or lognormal distributions, for example, the fit is not especially sensitive to a and b. In the four C_n^2 histograms in Figures 3–6, we used the same a and b values, $\ln\left(10^{-18}\right)$ and $\ln\left(10^{-12}\right)$, respectively. These are also the same values that Andreas (1989a) used. Likewise, for the four ℓ_0 histograms, we used the same limits, 0 and 20 mm. We conclude that the beta distribution is a useful tool for representing broad or narrow histograms that result from few or many data samples. And for our Arctic scintillometer data, the fit is fairly insensitive to the choices of a and b.

Although we have no theoretical justification for choosing the beta distribution, Harr (1987, p. 77 ff.), for example, provides ample practical justification. Briefly, with different choices of m and n, the beta distribution can be symmetric or skewed; it can approximate a normal or a lognormal distribution; and it can even represent a bathtub distribution.

The lognormal distribution is also commonly used to model propagation statistics (e.g., Ben-Yosef and Goldner 1988, Hill and Frehlich 1997). In particular, Frehlich (1992) found "satisfactory" agreement when he used the lognormal distribution to represent both C_n^2 and ℓ_0 measurements comprising 512 consecutive 4-s averages. For comparison, we thus plot autumn and spring C_n^2 histograms again in Figures 7 and 8 but now fitted with lognormal distributions.

Since the C_n^2 axes in Figures 7 and 8 are logarithmic, the plotted lognormal distributions are nearly symmetric. (Lognormal distributions plotted as continuous functions of C_n^2 would be perfectly symmetric; the need for bin-averaging in these plots distorts the symmetry a bit.) The actual C_n^2 histograms, however, are decidedly skewed. As a result, in both figures, the lognormal distribution underestimates the location of the peak in the histogram, underpredicts the occurrence of the larger C_n^2 values, and has an upper tail with too much area. Andreas (1989a) identified similar faults during comparisons of beta and lognormal fits of C_n^2 histograms. Thus, aside from computational ease, the lognormal distribution has nothing to recommend it over the beta distribution for fitting C_n^2 histograms.

Seasonal histograms of C_n^2 and ℓ_0, however, are not really our focus here; we, thus, present Figures 3–6 mainly to segue from Andreas's (1989a) work to ours and as background on using beta distributions for representing scintillation statistics. Here we necessarily concentrate instead on the short-term behavior of C_n^2 and ℓ_0 and find the beta distribution equally useful.
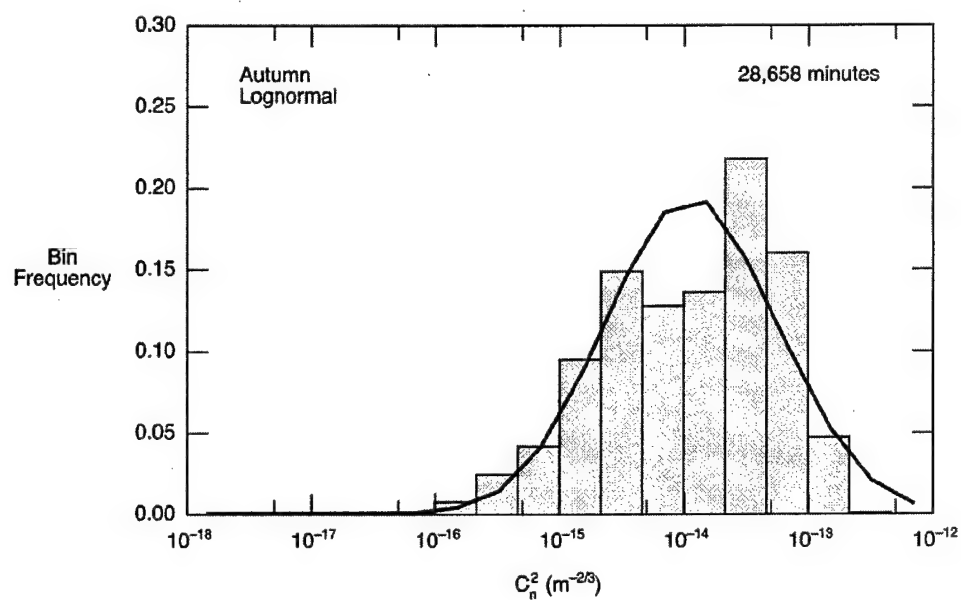
Figure 7. C_n^2 histogram from Figure 3, except here the solid curve is a lognormal distribution fitted to the histogram.
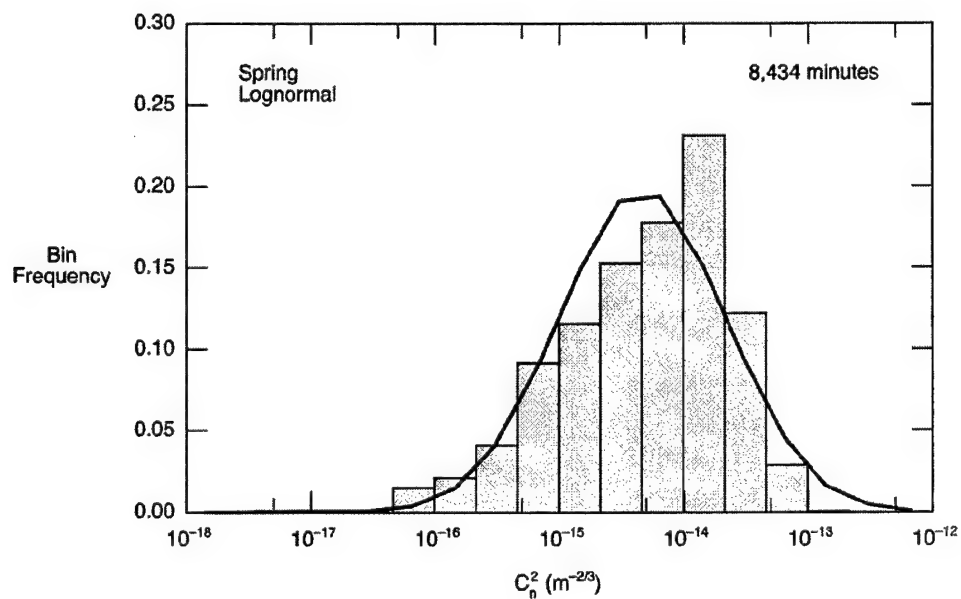
Figure 8. C_n^2 histogram from Figure 5, except here the solid curve is a lognormal distribution fitted to the histogram.

Figures 9–11 show histograms and beta distributions fitted to only one hour (i.e., 60 one-minute averages) of C_n^2 and ℓ_0 values for three different occasions. Later in the paper, we will base statistical analyses of these three periods on beta distributions. Therefore, we present Figures 9–11 to emphasize that beta distributions can fit both broad and narrow histograms comprising far fewer data points than in the seasonal histograms in Andreas (1989a) or in Figures 3–6.

To make Figures 9–11, we imposed the same lower and upper limits on both the C_n^2 and ℓ_0 distributions that we did in Figures 3–6. Yet even with these constant limits, the beta distribution is able to represent both wide (e.g., Figures 3, 5, and 11) and narrow (e.g., Figures 4, 9, and 10) histograms. This ability of the beta distribution with fixed lower and upper limits to capture the features of the histogram, even when there are few points, is important for our later analysis. Also, by fixing a and b for our C_n^2 and ℓ_0 analyses, we have essentially turned the beta distribution into a two-parameter model.

Another important feature of the beta distribution for our application is that it is bounded by a and b. The winter ℓ_0 histogram (i.e., Figure 4) looks bell shaped; we could have tried fitting it with a normal distribution. But given the sample mean and sample standard deviation of these winter ℓ_0 measurements, the normal distribution would have predicted a finite probability that ℓ_0 could be negative—a physical impossibility. By using a beta distribution for ℓ_0 and setting the a value to 0, we prevent this unphysical result.
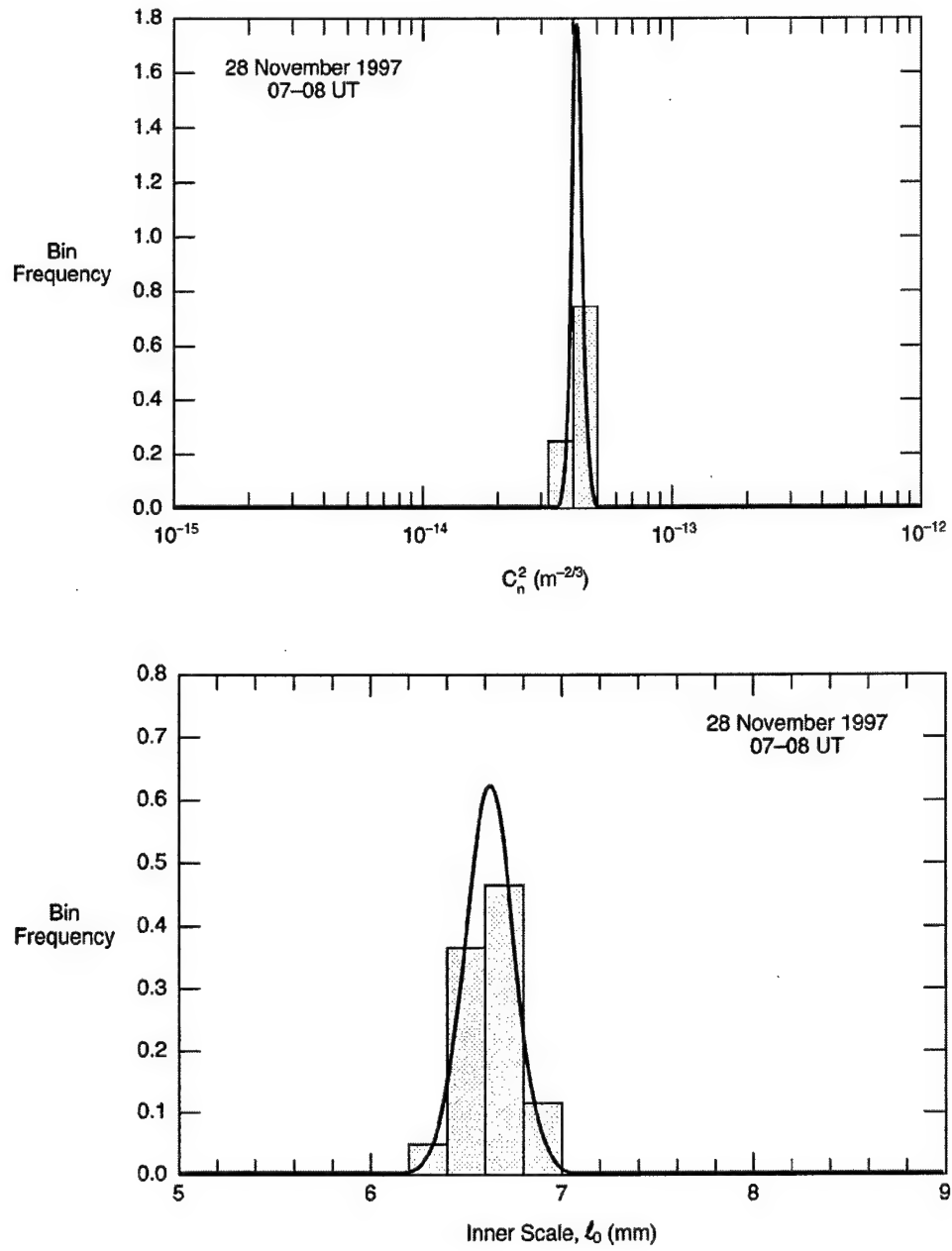
Figure 9. Histograms of 60 minute-averaged C_n^2 and ℓ_0 values measured at SHEBA between 07 and 08 UT on 28 November 1997. The solid curve is the beta distribution fitted to the histogram. In the C_n^2 plot, the lower and upper limits of the beta distribution, a and b, are $\ln(10^{-18}\ m^{-2/3})$ and $\ln(10^{-12}\ m^{-2/3})$, respectively; in the ℓ_0 plot, these limits are 0 and 20 mm.
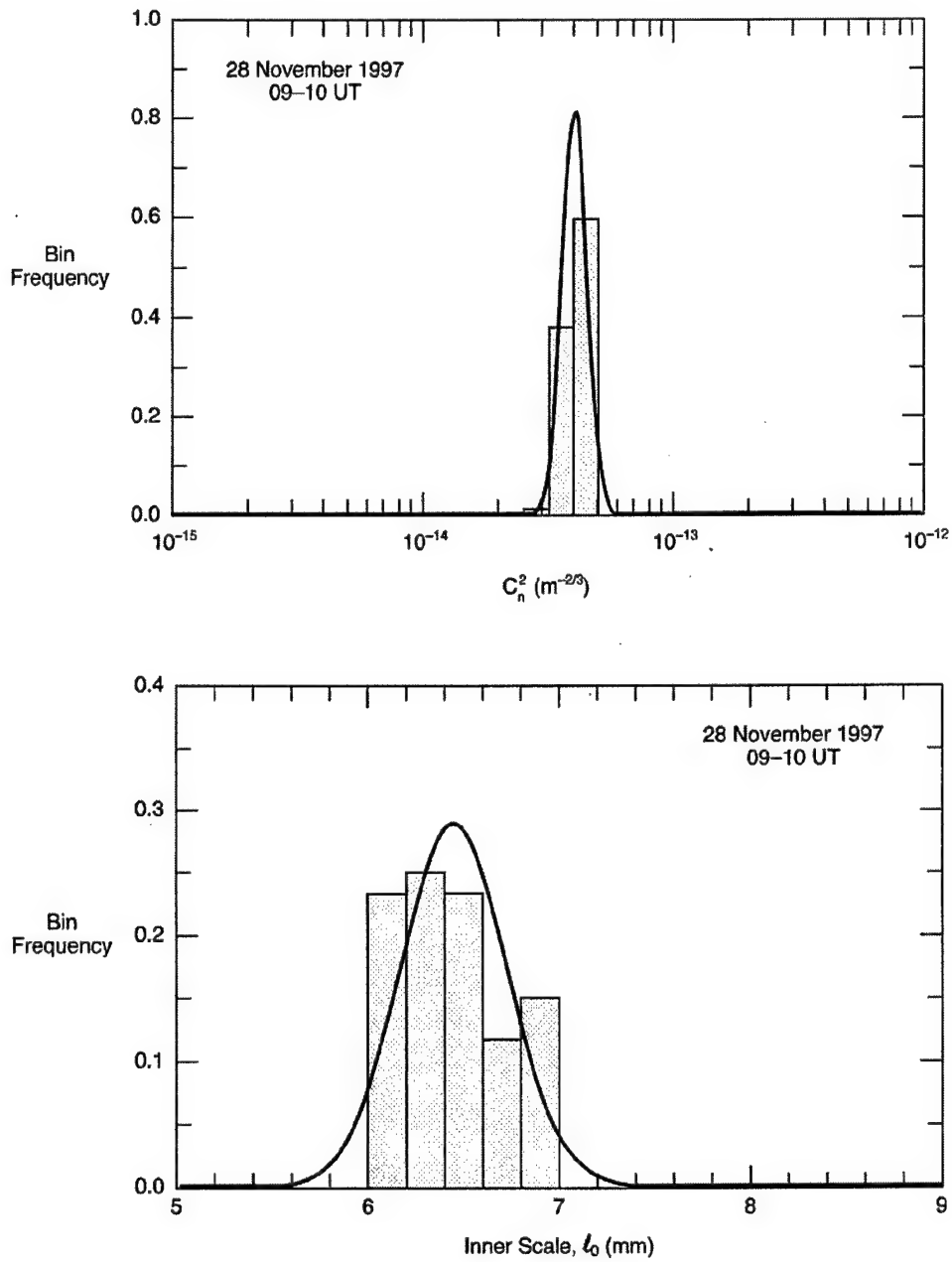
Figure 10. As in Figure 9, except these data are for 09–10 UT on 28 November 1997.
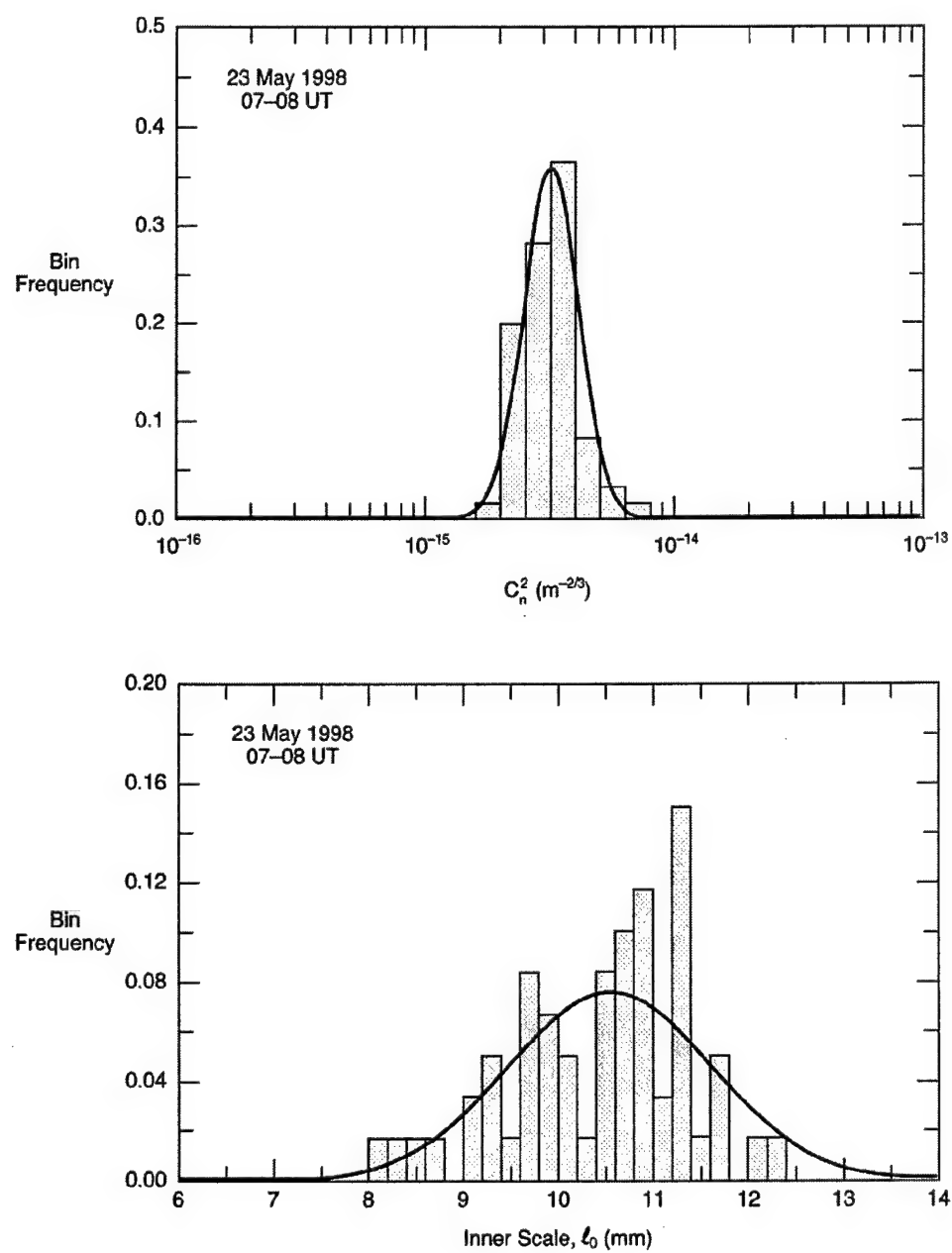
Figure 11. As in Figure 9, except these data are for 07–08 UT on 23 May 1998.

5 AVERAGING C_n^2 AND ℓ_0

With the knowledge that beta distributions can reliably represent histograms of C_n^2 and ℓ_0, we can set confidence intervals for measurements of C_n^2 and ℓ_0. In other words, we can investigate the role of averaging time in determining the confidence we have in various averages of C_n^2 and ℓ_0. Remember, the fundamental question we are researching is whether short-term averages of C_n^2 and ℓ_0 can yield meaningful estimates of u_* and H_s. Our view, again, is that, because of the need to use empirical similarity functions to compute these fluxes, the answer is "yes" only when the short-term measurements of C_n^2 and ℓ_0 faithfully represent the behavior of the C_n^2 and ℓ_0 time series over 30–60 minutes.

Define a time-dependent average X(t) and standard deviation s(t) as

$$X\left(t\right) = \frac{1}{N}\sum_{i=1}^{N}x_i \tag{5.1}$$

and

$$s^2\left(t\right) = \frac{1}{N-1}\left[\sum_{i=1}^{N}x_i^2 - NX^2\left(t\right)\right]. \tag{5.2}$$

Here x_i is the time series of minute averages of either C_n^2 or ℓ_0, $t = (N-1)\Delta t$, and Δt is one minute for our data. That is, X(t) and s(t) are the sample mean and sample standard deviation for all data in a time series from the first point to the Nth point, which corresponds to time t.

Figure 9 shows histograms for the C_n^2 and ℓ_0 values collected on 28 November 1997 between 07 and 08 UT. Figure 12 shows the hour-long time series of these minute-averaged C_n^2 and ℓ_0 values. The figure also includes the averages $C_n^2\left(t\right)$ and $\ell_0\left(t\right)$ computed with (5.1) between time zero and time t and 90% confidence intervals on the C_n^2 and ℓ_0 populations at each minute based on beta distributions computed from the average [X(t)] and the standard deviation [s(t)] of each variable at time t. [As before, for C_n^2, all statistics are based on $\ln\left(C_n^2\right)$.] The lower and upper limits of the beta distribution for C_n^2 here again correspond to 10^{-18} and 10^{-12} m$^{-2/3}$; for ℓ_0, the limits are again 0 and 20 mm.

Figure 12. Hour-long time series of the minute-averaged values of C_n^2 and ℓ_0 and averages of these computed from (5.1) from time zero until the 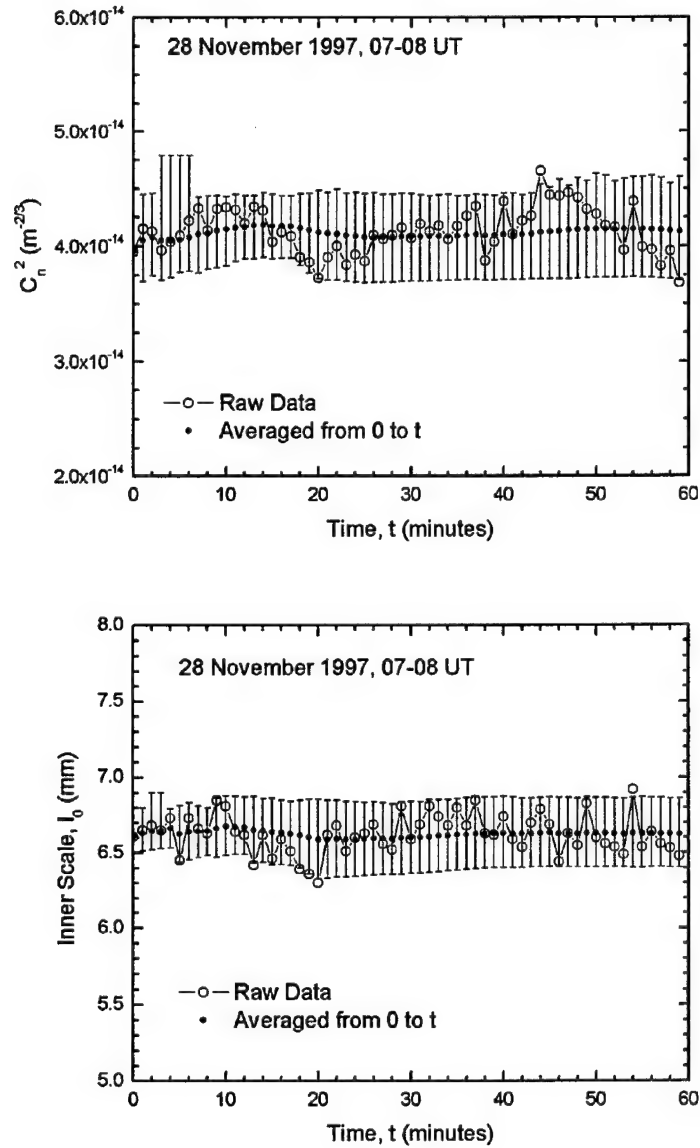plotted time, t. The errors bars show 90% confidence intervals based on a beta distribution computed from the average and standard deviation at time t [i.e., from (5.1) and (5.2)].

In Figure 12, we show 90% confidence intervals for the C_n^2 and ℓ_0 populations (as opposed to confidence intervals on the respective means) since these intervals represent the variability in the path-averaged atmosphere as observed by the scintillometer. Remember, our objective is to see how effective path-averaging instruments are in smoothing out nonstationarity or intermittency in the atmosphere.

Both the C_n^2 and ℓ_0 time series in Figure 12 support the contention that statistically meaningful values of these quantities can be obtained quite quickly. Here, after only 10 minutes of averaging, the 90% confidence intervals for both the C_n^2 and ℓ_0 populations bracket the respective averages for the remainder of the hour and also bracket almost all of the subsequent minute-averaged values. That is, the first 10 minutes of data faithfully represent all the C_n^2 and ℓ_0 values observed during the hour. For such series, using short-term averages of C_n^2 and ℓ_0—say 10-minute averages—to make inertial-dissipation estimates of u_* and H_s seems reasonable. Averaging C_n^2 and ℓ_0 for 30–60 minutes to match the averaging represented in the Monin–Obukhov similarity functions necessary for the inertial-dissipation estimates would not have changed the C_n^2 and ℓ_0 averages significantly.

To confirm this conclusion, we have estimated u_* and H_s from these time series using (1.5)–(1.7) and the similarity functions $g(\zeta)$ and $\phi_\varepsilon(\zeta)$ given in Appendix A. The averages of the first 10 minutes of C_n^2 and ℓ_0 values give u_* and H_s values of 0.0745 m s^{-1} and –6.68 W m^{-2}, respectively, while the C_n^2 and ℓ_0 averages for the entire 60-minute series yield values of 0.0754 m s^{-1} and –6.78 W m^{-2}. That is, the differences here between fluxes based on 60-minute averages and averages of only the first 10 minutes of the series are about 1% for both u_* and H_s. In fact, the u_* and H_s values computed from the C_n^2 and ℓ_0 averages for each 10-minute block within these 60-minute series are within about 3% of the u_* and H_s values computed from the hourly averages of C_n^2 and ℓ_0. Again, these results support the premise that path-averaging instruments provide accurate estimates of the surface fluxes quickly.

The histograms in Figure 10 and the time series in Figure 13, however, present a different situation just two hours later. During this hour, C_n^2 has a downward trend, while ℓ_0 has an upward trend. Both series also show shorter periods of nonstationarity. As a result, the 90% confidence interval for the C_n^2 population calculated from 10 minutes of data brackets fewer than half of the subsequent minute averages and does not even include the C_n^2 average at the end of the hour. Likewise, the 90% confidence interval for the ℓ_0 population obtained from 10 minutes of averaging brackets fewer than half of the subsequent minute averages of ℓ_0 and barely includes the ℓ_0 average at the end of the hour.

In other words, for the data in Figures 10 and 13, 10 minutes of averaging does not faithfully predict the variability of the C_n^2 and ℓ_0 values that occur during this hour.
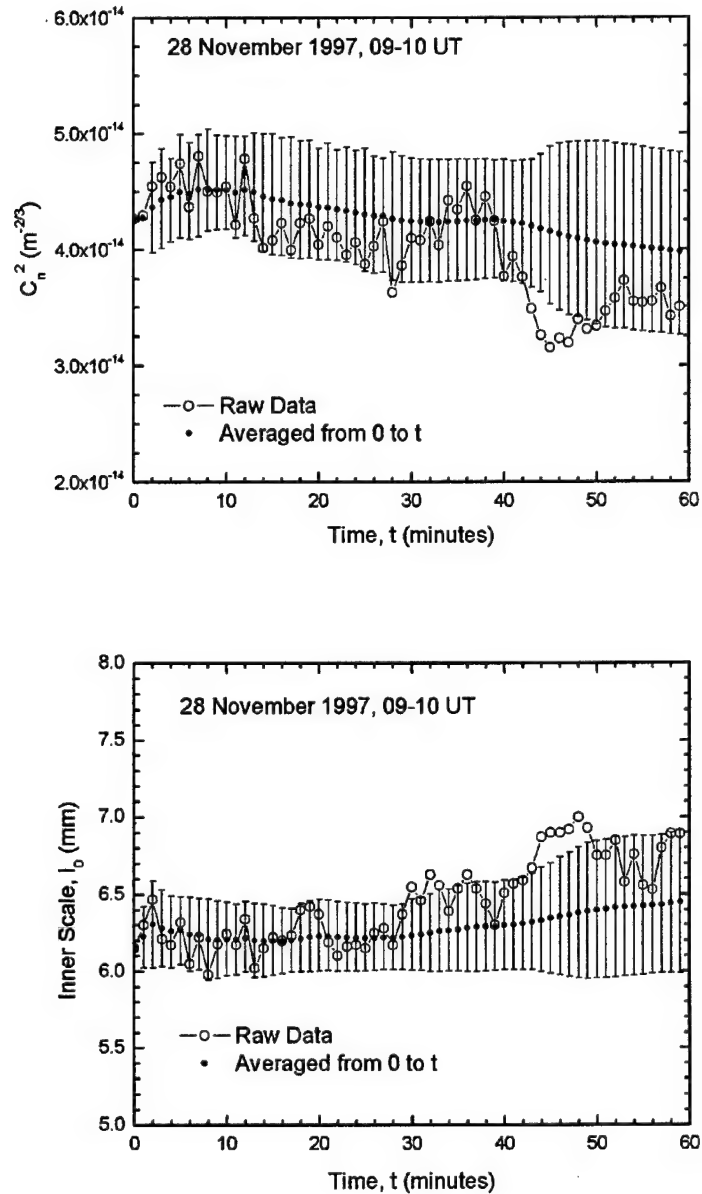

Figure 13. As in Figure 12 but two hours later.

This example thus refutes the hypothesis that short-term averages of C_n^2 and ℓ_0 can, in general, yield meaningful estimates of the surface momentum and sensible heat fluxes. Here, because of the nonstationarity, it is not obvious that short-term C_n^2 and ℓ_0 averages can be meaningfully convolved with functions based on 30–60 minutes of averaging. In essence, nonstationarity can confound path-averaging sensors just as it confounds point sensors.

To demonstrate, we again compare u_* and H_s values computed from the first 10 minutes of these C_n^2 and ℓ_0 series and from the entire series. C_n^2 and ℓ_0 averages for the first 10 minutes yield u_* and H_s values of 0.0844 m s^{-1} and –8.18 W m^{-2}, respectively, while the 60-minute averages yield values of 0.0795 m s^{-1} and –7.18 W m^{-2}. These u_* values differ by 6.1%, while the H_s values differ by 13.9%. The fourth 10-minute block in these series produced worse results; the u_* and H_s values based on these 10-minute averages differ from values based on the 60-minute averages by 7.8% and 15.6%, respectively.

While these differences in the H_s estimate, in particular, are not large in magnitude, the percentage differences are significant. In mid-latitudes, over land, where H_s can be 200–300 W m^{-2}, for example, a 15% uncertainty in H_s amounts to 30–45 W m^{-2}. Such an uncertainty is much too large if we have intentions, for instance, to ever use scintillation to improve climatological estimates of the surface heat budget, where an accuracy of 5–10 W m^{-2} is essential (e.g., Mitchell 1989, Kiehl and Trenberth 1997).

Figure 14 shows another hour of C_n^2 and ℓ_0 values from May 1998 to emphasize these points. (The corresponding histograms are in Figure 11.) In contrast to Figure 13, the C_n^2 and ℓ_0 time series here do not have trends but do display a lot of variability. As a result, although the confidence interval on the C_n^2 population at 10 minutes brackets all subsequent C_n^2 averages, it brackets only about half of the subsequent minute averages. The situation is not quite as bad for the ℓ_0 series, mainly because variability early in the series leads to a large 90% confidence interval for the population after 10 minutes of averaging. Still, 20% of the subsequent minute-averaged ℓ_0 values are outside this 90% confidence interval. And the confidence interval for the population after an hour of averaging is 25% larger than the confidence interval at 10 minutes.

Hence, again 10 minutes of scintillometer data did not provide a very accurate picture of the C_n^2 and ℓ_0 populations we encountered during this hour. Therefore, it does not seem prudent to use, say, the 10-minute-averaged C_n^2 and ℓ_0 values from these series in inertial-dissipation estimates of the surface fluxes. The nonstationarity leads to confidence intervals for the C_n^2 and ℓ_0 populations with widths that are significant fractions of the respective mean values: about

35% for C_n^2 and about 17% for ℓ_0 after an hour of averaging. We would, again, not be making very reliable estimates of the surface fluxes.
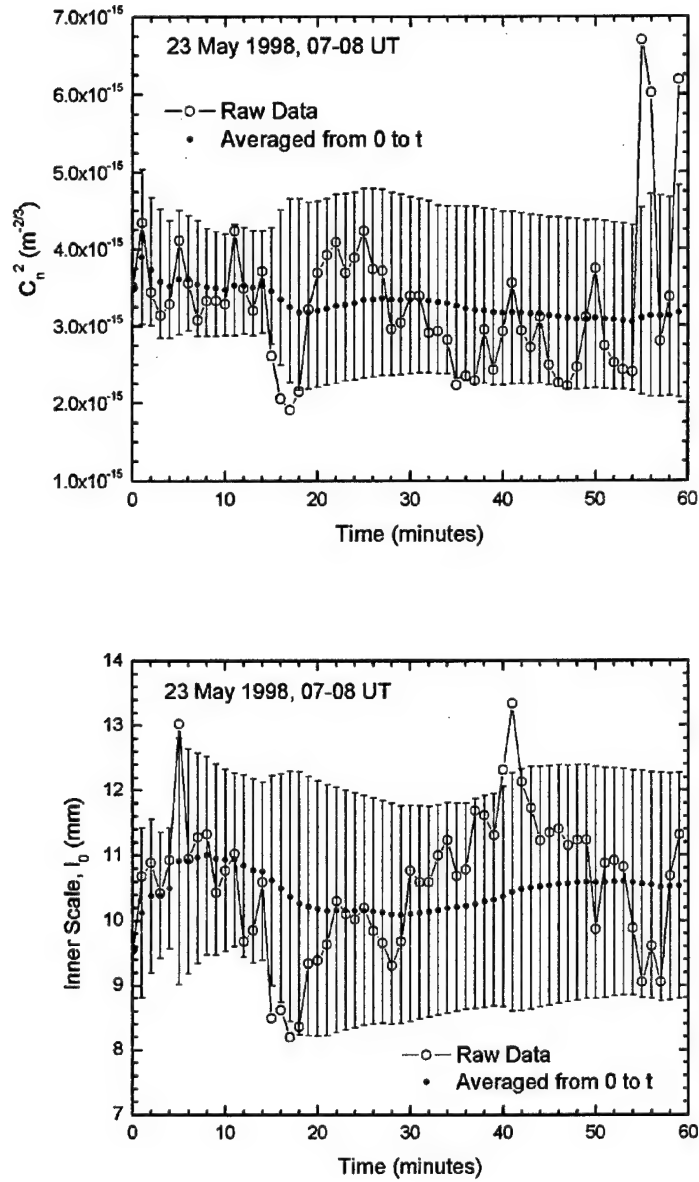
Figure 14. As in Figure 12 but in May 1998.

To confirm this conclusion, we again compare calculations of u_* and H_s based on the first 10 minutes of these C_n^2 and ℓ_0 times series and on the entire 60-minute series. The first 10 minutes yields u_* and H_s values of 0.0451 m s^{-1} and −1.32 W m^{-2}, respectively, while the 60-minute C_n^2 and ℓ_0 averages yield values of 0.0488 m s^{-1} and −1.42 W m^{-2}. These values differ by 7–8%. Averages of C_n^2 and ℓ_0 from the second 10-minute block in these series, however, yield u_* and H_s values that differ from the 60-minute averages by 22% and 24%, respectively. These are large excursions from the long-term means despite the fact that these data from 10–19 minutes were also used to compute the 60-minute averages.

The idea that path-averaging instruments can yield meaningful estimates of turbulent surface fluxes in a fraction of the time that point measurements can springs from the hope that the path-averaging would quickly sample enough turbulent eddies to minimize the effects of nonstationarity. As Figures 13 and 14 demonstrate, for propagation paths of 300–350 m at least, this does not happen in general. Nonstationarity is still a problem for path-averaging instruments.

6   QUANTIFYING THE NONSTATIONARITY

Since nonstationarity turns out to present sampling problems for path-averaging sensors as well as for point sensors, we use our scintillometer data to study ways to quantify this nonstationarity. Mahrt (1998) defines a "non-stationarity ratio" just for this purpose. We adapt his method to our data.

Again, let x represent the minute-averaged time series of C_n^2 or ℓ_0 values. Consider an hour series that, thus, includes 60 of these values. Block these 60 values into I records of J samples each. The x series thus now has two subscripts, i and j (i.e., x_{ij}), where i goes from 1 to I and j goes from 1 to J.

Mahrt (1998) defines the "within-record" standard deviation of x for record i as

$$s_{wi,i} = \left[\frac{1}{J-1} \sum_{j=1}^{J} \left(x_{ij} - \overline{x}_i \right)^2 \right]^{1/2} , \qquad (6.1)$$

where

$$\overline{x}_i = \frac{1}{J} \sum_{j=1}^{J} x_{ij} . \qquad (6.2)$$

He then averages $s_{wi,i}$ over the I records to obtain one estimate of the within-record standard deviation,

$$s_{wi} = \frac{1}{I} \sum_{i=1}^{I} s_{wi,i} . \qquad (6.3)$$

From this statistic, he defines the random error as

$$RE = s_{wi} / J^{1/2} . \qquad (6.4)$$

Mahrt (1998) next defines the "between-record" standard deviation as

$$s_{btw} = \left[\frac{1}{I-1} \sum_{i=1}^{I} \left(\overline{x}_i - \overline{x} \right)^2 \right]^{1/2} , \qquad (6.5)$$

where

$$\bar{x} = \frac{1}{I}\sum_{i=1}^{I}\bar{x}_i = \frac{1}{IJ}\sum_{i=1}^{I}\sum_{j=1}^{J}x_{ij} \ . \tag{6.6}$$

Clearly, in our analysis, $IJ = 60$. Mahrt's nonstationarity ratio is then just

$$NR = \frac{s_{btw}}{RE} = \frac{J^{1/2}\,s_{btw}}{s_{wi}} \ . \tag{6.7}$$

Conceptually, s_{btw} is large when nonstationarity produces long segments of the series that remain above or below the series mean, as in both the C_n^2 and ℓ_0 series in Figure 13. On the other hand, s_{wi} is large and NR tends to be smaller when the time series has a great deal of random variability, as in the C_n^2 plot in Figure 14. Thus, Mahrt's (1998) nonstationarity ratio compares the effects of coherent behavior with the inherent variability in the time series. According to Mahrt, "for stationary conditions, NR is approximately unity." NR values significantly larger than one reflect nonstationarity.

We have calculated NR twice each for the raw 60-minute C_n^2 and ℓ_0 time series plotted in Figures 12–14 to see if this ratio can complement our analysis in the previous section. In one case, $I = 6$ and $J = 10$; and in the second case, $I = 10$ and $J = 6$. Table 1 summarizes the results.

The first thing we notice in the table is that the NR values calculated for the two I–J pairings are not necessarily the same. For the C_n^2 and ℓ_0 traces in Figures 12 and 14, the respective NRs for the two I–J pairs are similar, if not identical. But for Figure 13, the NRs for C_n^2, 7.05 and 5.27, and for ℓ_0, 6.54 and 5.36, each differ by over 20%. Mahrt (1998) does not suggest any obvious guidelines for choosing I or J; but from the basis for his method, we believe that J should represent a period that is typical of the large-scale variability in the signal. The C_n^2 and ℓ_0 traces in Figure 13 have large-scale coherence for periods longer than 6 minutes. As a result, the $J = 10$ and $J = 6$ calculations yield significantly different results for these series.

On the other hand, the nonstationarity ratios listed in Table 1 both confirm some of our previous conclusions that we based on confidence intervals and contrast with them. For example, the C_n^2 and ℓ_0 traces in Figure 12 are well behaved, and we had concluded that short-term averages from these series would be useful for estimating fluxes. Likewise, the NR values for these series for both I–J pairs are consistent and are two of the three smallest collections in the table.

In particular, the NRs for the ℓ_0 series, 1.6–1.7, are near one, the value Mahrt (1998) associates with a stationary time series.

Table 1. Calculations of the nonstationarity ratio, NR, from (6.7) for the raw C_n^2 and ℓ_0 series shown in Figures 12–14 for two choices of I and J. "Average" denotes the one-hour average. "Crossings" counts the number of times the series crosses this average. "59/Crossings" is another measure of nonstationarity explained in the text.

	28 Nov 1997 07–08 UT (Figure 12)	28 Nov 1997 09–10 UT (Figure 13)	23 May 1998 07–08 UT (Figure 14)
C_n^2			
Average (m$^{-2/3}$)	4.14×10^{-14}	4.01×10^{-14}	3.27×10^{-15}
NR I = 6, J = 10 I = 10, J = 6	2.75 2.97	7.05 5.27	2.23 2.23
Crossings	20	9	18
59/Crossings	2.95	6.55	3.28
ℓ_0			
Average (mm)	6.62	6.45	10.54
NR I = 6, J = 10 I = 10, J = 6	1.63 1.68	6.54 5.36	3.77 3.35
Crossings	22	7	13
59/Crossings	2.68	8.43	4.54

The nonstationarity ratios also corroborate our evaluation of the C_n^2 and ℓ_0 series in Figure 13. These both had unacceptable short-term behavior, largely because of their trends; and the NRs for these are the four largest values in the table. Evidently, if a series is stationary, the choice of I and J is not too crucial:

Both I–J pairs yielded comparable NR values for both the C_n^2 and ℓ_0 traces in Figure 12. But when a series is nonstationary, as is Figure 13, different choices for I and J can yield markedly different values of NR. These NR values, nevertheless, are large and do suggest what they should—that the series is nonstationary.

Lastly, the nonstationarity ratios for the C_n^2 and ℓ_0 series in Figure 14 suggest conclusions that contrast with our earlier discussion of these series. We had also judged these two series unreliable for producing short-term averages because of their large variability. The NRs of the C_n^2 series in Figure 14, however, both 2.23, are smaller than the NR of the supposedly "good" C_n^2 series in Figure 12. And the NR values for the ℓ_0 series, 3.77 and 3.35, are larger than the NRs for the C_n^2 series, although we had earlier concluded that the ℓ_0 series in Figure 14 was "better" for averaging than the C_n^2 series on the basis of our uncertainty analysis. These discrepancies raise questions about what nonstationarity means in general and what Mahrt's (1998) nonstationarity ratio quantifies in particular.

In reviewing (6.1)–(6.7), we see that NR, through its linear dependence on the between-record variability, s_{btw}, tends to be large if coherent sections of the record are above or below the mean. On the other hand, because of its inverse dependence on within-record variability, s_{wi}, NR tends to be small if the time series has large-amplitude random variability. The C_n^2 trace in Figure 14 has such large-amplitude variability (i.e., large s_{wi}), but the events are not necessarily coherent (i.e., small s_{btw}). As a result, the NR for this series is relatively small despite error bars that increase with time. The ℓ_0 trace in Figure 14, in contrast, has large-amplitude variability (i.e., large s_{wi}), but that variability is more coherent. There are, essentially, four segments in the time series: two above and two below the mean. Thus, s_{btw} is also large, and this combination yields mid-range NRs that are larger than the NRs for the C_n^2 series.

In summary, according to Mahrt's (1998) definition of nonstationarity, as formalized in his nonstationarity ratio NR, two effects contribute most to nonstationarity: a trend, and large, coherent excursions from the mean. By "large" here, we mean events that span a significant fraction of the time series, say 10% of it. We are tempted to call such events "intermittency," but the definition of this term in the new *Glossary of Meteorology* (Glickman 2000) does not seem to fit our description. Consequently, we will simply call these nonstationary events.

Again according to Mahrt (1998), large-amplitude, random variability is the opposite of nonstationarity: This variability actually reduces his nonstationarity ratio. In essence, if a series is highly variable, coherent excursions from the mean should not be surprising and, thus, should not be judged as nonstationarity. In

our uncertainty-based analysis, however, such highly variable series lead to wide confidence intervals and, in turn, to uncertain estimates of the surface fluxes. In other words, nonstationarity (at least as defined by Mahrt) is not the sole cause of uncertain flux estimates: Random variability also leads to uncertainty.

These insights into Mahrt's (1998) nonstationarity ratio led us to realize that, generally, a stationary time series exhibits many zero-crossings, while a non-stationary series has long segments above or below zero. (Here, zero-crossings refer to a series with the mean removed.) Table 1 also lists the number of zero-crossings for the raw C_n^2 and ℓ_0 series in Figures 12–14, where that count includes both up-going and down-going zero-crossings. These counts mirror our analysis based on NR. The C_n^2 and ℓ_0 series in Figure 12 have many crossings and small NR; the series in Figure 13 have few crossings and large NR; and the series in Figure 14 have intermediate numbers of crossings and, generally, intermediate NR.

A series of 60 samples can cross zero at most 59 times and must cross zero at least once. Denote the number of crossings as C and this maximum number of crossings as M. Clearly, $1 \leq M/C \leq M$. Mahrt's (1998) NR, in contrast, is not necessarily always greater than or equal to one. Although Mahrt states that his NR is "approximately" one for a stationary series, we have created artificial series with NR less than one (for example, a 60-point square wave of amplitude 1 and wavelength 12). It seems useful to have a nonstationarity metric with obvious lower and upper limits. In counting zero-crossings, $M/C = 1$ would mean that each consecutive point switches from above to below the mean or vice versa. This behavior is a good indication that the series is stationary. In contrast, $M/C = M$ would mean the series crosses zero only once and, thus, has a trend.

The M/C values in Table 1 (i.e., "59/Crossings") are similar in both magnitude and trend to the corresponding NRs and, therefore, seem to be a nonstationarity metric that is as good as NR. Counting zero-crossings is also much easier than making the calculations necessary to evaluate NR. Another benefit is that counting zero-crossings obviates the need to make arbitrary choices of I and J.

To develop a better sense of what this zero-crossing metric tells us about a time series, we computed M/C for hourly intervals of the C_n^2 and ℓ_0 time series in Figure 2. Figure 15 shows the results.
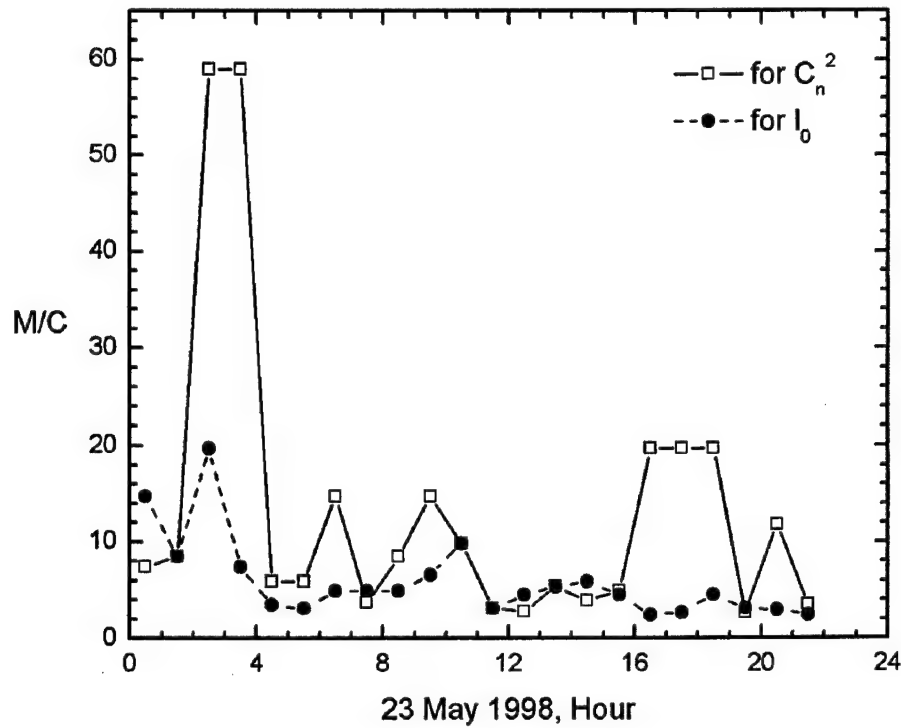
Figure 15. The nonstationarity metric M/C for hourly segments of the C_n^2 and ℓ_0 time series in Figure 2, where M is always 59 (= 60 − 1) and C counts the zero-crossings during the hour. Values are plotted at the mid-point of the hour. Because during the last two hours the series in Figure 2 had gaps, we calculated no M/C values for these hours.

The first thing this figure suggests is that, on this day, C_n^2 was much more nonstationary than ℓ_0 was. In fact, between 02 and 04 UT, when C_n^2 climbed steadily through two orders of magnitude (see Figure 2), its M/C value was at its maximum, 59. That is, C_n^2 had only one zero-crossing each hour. During the steady decline from 16 to 19 UT in Figure 2, C_n^2 also had large M/C values, almost 20 (i.e., 3 zero-crossings during each hour).

The largest M/C value for the ℓ_0 record in Figure 2 also occurs for 02–03 UT, when ℓ_0 is climbing out of its local minimum. The ℓ_0 record also has large M/C values for 00–01 UT and 10–11 UT, when ℓ_0 undergoes some large, coherent excursions. We conclude from Figure 15 that M/C is a good indicator of a trend in a time series and of coherent excursions on either side of the mean.

Finally, Figure 15 suggests that C_n^2 and ℓ_0 were both stationary during the five-hour period 11–16 UT. Here, the M/C values for both C_n^2 and ℓ_0 are

between 2 and 6. Likewise, the C_n^2 and ℓ_0 traces in Figure 2 show fairly constant levels here and more modest fluctuations than in the rest of the records. We thus recommend considering a time series to be stationary if M/C is less than 6.

7   CONCLUSIONS

Our SHEBA scintillometer data confirm Andreas's (1989a) conclusion that a beta distribution with lower and upper limits corresponding to 10^{-18} and 10^{-12} m$^{-2/3}$ reliably models the distribution of Arctic near-surface C_n^2 values. We are, evidently, the first to report that a beta distribution with lower and upper limits of 0 and 20 mm is also useful for representing values of the inner scale of turbulence, ℓ_0.

Using this knowledge of the sampling distributions for C_n^2 and ℓ_0, we have investigated the question of whether short-term averages of path-averaged C_n^2 and ℓ_0 values can yield reliable estimates of the surface stress and the surface sensible heat flux through an inertial-dissipation calculation. The answer turns on the fact that the similarity functions used in the inertial-dissipation calculations derive from point measurements based on averages of 30–60 minutes. The cautious approach is to convolve short-term averages of C_n^2 and ℓ_0 (i.e., on the order of minutes) with these similarity functions only if short records of C_n^2 and ℓ_0 fairly represent the behavior of time series over 30–60 minutes.

Our analyses of three typical hour-long time series of C_n^2 and ℓ_0 measurements from SHEBA imply that path-averaging confers no general benefits when the objective is to shorten the averaging time for flux sampling. Short-term series simply do not always bracket the behavior of 30–60 minute series. If the C_n^2 and ℓ_0 time series, however, are stationary over, say, hourly intervals, the fluxes of heat and momentum computed over 10-minute subrecords can be statistically reliable. That is, for stationary series, it is safe to convolve short-term C_n^2 and ℓ_0 averages with similarity functions derived from longer averaging.

But nonstationarity leads to uncertain flux measurements with path-averaging instruments just as it does for point measurements, at least for averaging paths of 300–350 m. On the basis of our three examples and the averaging estimates we reviewed in Section 3, we expect estimates of τ and H_s to easily vary by 20% or more between adjacent 10-minute subrecords. This is the random error resulting from variability in C_n^2 and ℓ_0. Estimates of τ and H_s could also suffer from bias errors caused by using similarity functions unproven for short-term averaging. Admittedly though, in some applications, both errors may be tolerable.

In our view, the best way to ensure reliable short-term flux estimates from scintillometer data is to first validate the Monin–Obukhov similarity functions from measurements of short-term averages. That is, make point measurements of, say, 10-minute averages of the vertical wind speed and temperature gradients and

the fluxes $\overline{uw}$ and $\overline{wt}$ and see how well these data fit known functions for $\phi_\varepsilon(\zeta)$ and $g(\zeta)$. Though the computed functions will be quite scattered, perhaps we will see the same $\phi_\varepsilon(\zeta)$ and $g(\zeta)$ functions emerging that longer averaging has yielded. If so, the experiment establishes the validity of Monin–Obukhov similarity for short-term averages and puts scintillometer flux analysis on firm theoretical and experimental footing. To our knowledge, however, this experiment has never been done, and there are no guarantees that it will work. As Wyngaard (1973, p. 41) emphasizes and as the discussion in Section 3 demonstrates, "Nature, not man, determines what is short-term."

Because nonstationarity turned out to be one key for deciding whether a flux estimate was reliable, we evaluated two metrics for quantifying nonstationarity. Mahrt's (1998) nonstationarity ratio tended to corroborate our analysis of the utility of C_n^2 and ℓ_0 for estimating fluxes that we based on assigning confidence intervals. That is, acceptable C_n^2 and ℓ_0 series generally had small values of NR, while unacceptable series had larger NRs. We did identify some examples that went against intuition, however. These series had large-amplitude, random variability and, thus, produced averages with large uncertainty; still, their NRs were fairly small. One manifestation of nonstationarity is, thus, extended segments of the series either above or below the mean. High random variability, on the other hand, is the opposite of nonstationarity but still degrades flux estimates.

In light of these insights, we realized that the number of zero-crossings, C, in a series is another useful measure of nonstationarity. A benefit of this metric is that a series of M+1 data points can display no more than M zero-crossings and must have at least one zero-crossing. Consequently, M/C can have values only from 1 to M. When it is 1, consecutive points in the series just switch back and forth between positive and negative—an obviously stationary series. When it is M, the series crosses zero only once because of a strong trend. Mahrt's (1998) nonstationarity ratio, on the other hand, does not have obvious limiting values, depends sensitively on choices of the blocking values I and J, and requires more elaborate calculations than simply counting zero-crossings. Finally, in our six examples, the M/C values are remarkably near the corresponding NRs. M/C is thus another simple measure of nonstationarity.

APPENDIX A: THE SIMILARITY FUNCTIONS g(ζ) AND ϕ_ε(ζ)

Hill (1997) provides an authoritative review of the algorithms and similarity functions necessary to compute u_* and t_* from scintillation statistics. Although the similarity functions g(ζ) and ϕ_ε (ζ) that we use in (1.6) and (1.7) are not necessarily his "preferences," no data set has yet proved sufficient to distinguish significant differences between his choices and ours.

For ϕ_ε, we use

$$\phi_\varepsilon(\zeta) = \left[1 + 0.46(-\zeta)^{2/3}\right]^{3/2} \tag{A1}$$

in unstable stratification ($\zeta \le 0$) and

$$\phi_\varepsilon(\zeta) = \left[1 + 2.3\zeta^{3/5}\right]^{3/2} \tag{A2}$$

in stable stratification ($\zeta \ge 0$). These functions are from Wyngaard and Coté (1971), but Andreas (1988b) modified their original coefficients to reflect a von Kármán constant of 0.40 rather than the 0.35 that they assumed. Here also,

$$\zeta = \frac{z}{L} = \frac{k z \hat{g}}{T_v} \frac{t_*}{u_*^2} , \tag{A3}$$

where L is the Obukhov length, $\hat{g}$ is the acceleration of gravity, and T_v is the average virtual temperature.

Stable stratification is a special concern of ours in this SHEBA data set. Andreas (1998, 2002) and Jordan et al. (1999) discuss the Monin–Obukhov similarity functions for stable stratification and recommend the so-called "Dutch" formulation (Holtslag and De Bruin 1988) for the dimensionless temperature profile function,

$$\phi_h(\zeta) = 1 + 0.7\zeta + 0.75\zeta(6 - 0.35\zeta)\exp(-0.35\zeta). \tag{A4}$$

This has the best properties among the available ϕ_h functions in very stable stratification (Andreas 2002). We can incorporate the desirable properties of this function into our g(ζ) equation by using the expression for g(ζ) that Andreas (1988b) derives from the scalar variance budget. That is,

$$g(\zeta) = \frac{5.92\phi_h(\zeta)}{\phi_\varepsilon^{1/3}(\zeta)} , \qquad\qquad (A5)$$

where, for stable stratification, we use (A2) for ϕ_ε and (A4) for ϕ_h.

In unstable stratification, we use (Edson and Fairall 1998)

$$g(\zeta) = 5.92(1 - 8\zeta)^{-2/3} \qquad\qquad (A6)$$

because it matches (A5) best at $\zeta = 0$.

REFERENCES

Abramowitz, M., and I. A. Stegun (Eds.) (1965) *Handbook of Mathematical Functions.* New York: Dover, 1046 p.

Andreas, E. L (1987) On the Kolmogorov constants for the temperature–humidity cospectrum and the refractive index spectrum. *Journal of the Atmospheric Sciences,* **44,** 2399–2406.

_____ (1988a) Estimating averaging times for point and path-averaged measurements of turbulence spectra. *Journal of Applied Meteorology,* **27,** 295–304.

_____ (1988b) Estimating C_n^2 over snow and sea ice from meteorological data. *Journal of the Optical Society of America A,* **5,** 481–495.

_____ (1989a) The refractive index structure parameter, C_n^2, for a year over the frozen Beaufort Sea. *Radio Science,* **24,** 667–679.

_____ (1989b) Two-wavelength method of measuring path-averaged turbulent surface heat fluxes. *Journal of Atmospheric and Oceanic Technology,* **6,** 280–292.

_____ (Ed.) (1990) *Selected Papers on Turbulence in a Refractive Medium.* SPIE MS 25. Bellingham, Washington: Society of Photo-Optical Instrumentation Engineers, 693 p.

_____ (1992) Uncertainty in a path-averaged measurement of the friction velocity u_*. *Journal of Applied Meteorology,* **31,** 1312–1321.

_____ (1998) The atmospheric boundary layer over polar marine surfaces. *Physics of Ice-Covered Seas,* Vol. 2, M. Leppäranta, Ed., Helsinki: Helsinki University Press, 715–773.

_____ (2002) Parameterizing scalar transfer over snow and ice, A review. *Journal of Hydrometeorology,* **3,** 417–432.

_____, **and B. A. Cash** (1996) A new formulation for the Bowen ratio over saturated surfaces. *Journal of Applied Meteorology,* **35,** 1279–1289.

_____, **C. W. Fairall, P. S. Guest, and P. O. G. Persson** (1999) An overview of the SHEBA atmospheric surface flux program. Preprints, *Fifth Conference on Polar Meteorology and Oceanography,* Dallas, Texas, Boston: American Meteorological Society, 411–416.

____, ____, **P. O. G. Persson, and P. S. Guest** (2000) Probability distributions for scintillometer-derived values of the inner scale and the refractive index structure parameter and their implications for averaging. Preprints, *14th Symposium on Boundary Layers and Turbulence*, Aspen, Colorado, Boston: American Meteorological Society, 19–22.

____, ____, ____, and ____ (2003) Probability distributions for the inner scale and the refractive index structure parameter and their implications for flux averaging. *Journal of Applied Meteorology*, **42**, 1316–1329.

Arya, S. P. (1988) *Introduction to Micrometeorology*. San Diego: Academic Press, 307 p.

Ben-Yosef, N., and E. Goldner (1988) Splitting-source model for the statistics of irradiance scintillations. *Journal of the Optical Society of America A*, **5**, 126–131.

Businger, J. A., J. C. Wyngaard, Y. Izumi, and E. F. Bradley (1971) Flux-profile relationships in the atmospheric surface layer. *Journal of the Atmospheric Sciences*, **28**, 181–189.

Chernov, L. A. (1967) *Wave Propagation in a Random Medium*. New York: Dover, 168 p.

De Bruin, H. A. R., B. J. J. M. van den Hurk, and W. Kohsiek (1995) The scintillation method tested over a dry vineyard area. *Boundary-Layer Meteorology*, **76**, 25–40.

____, **W. M. L. Meijninger, A.-S. Smedman, and M. Magnusson** (2002) Displaced-beam small aperture scintillometer test. Part I: The WINTEX data-set. *Boundary-Layer Meteorology*, **105**, 129–148.

Dyer, A. J., and E. F. Bradley (1982) An alternative analysis of flux-gradient relationships at the 1976 ITCE. *Boundary-Layer Meteorology*, **22**, 3–19.

Edson, J. B., and C. W. Fairall (1998) Similarity relationships in the marine atmospheric surface layer for terms in the TKE and scalar variance budgets. *Journal of the Atmospheric Sciences*, **55**, 2311–2328.

____, ____, **P. G. Mestayer, and S. E. Larsen** (1991) A study of the inertial-dissipation method for computing air–sea fluxes. *Journal of Geophysical Research*, **96**, 10,689–10,711.

Fairall, C. W., and S. E. Larsen (1986) Inertial-dissipation methods and turbulent fluxes at the air–ocean interface. *Boundary-Layer Meteorology*, **34**, 287–301.

Frederickson, P. A., K. L. Davidson, C. R. Zeisse, and C. S. Bendall (2000) Estimating the refractive index structure parameter (C_n^2) over the ocean using bulk methods. *Journal of Applied Meteorology*, **39**, 1770–1783.

Frehlich, R. G. (1988) Estimation of the parameters of the atmospheric turbulence spectrum using measurements of the spatial intensity covariance. *Applied Optics*, **27**, 2194–2198.

_____ (1992) Laser scintillation measurements of the temperature spectrum in the atmospheric surface layer. *Journal of the Atmospheric Sciences*, **49**, 1494–1509.

Glickman, T. S. (Ed.) (2000) *Glossary of Meteorology*. 2nd ed. Boston: American Meteorological Society, 855 p.

Gray, D. A., and A. T. Waterman, Jr. (1970) Measurement of fine-scale atmospheric structure using an optical propagation technique. *Journal of Geophysical Research*, **75**, 1077–1083.

Green, A. E., K. J. McAneney, and M. S. Astill (1994) Surface-layer scintillation measurements of daytime sensible heat and momentum fluxes. *Boundary-Layer Meteorology*, **68**, 357–373.

Gurvich, A. S., N. S. Time, L. S. Turovtseva, and V. F. Turchin (1974) Reconstruction of the temperature fluctuation spectrum of the atmosphere from optical measurements. *Izvestia, Atmospheric and Oceanic Physics*, **10**, 292–297.

Harr, M. E. (1987) *Reliability-Based Design in Civil Engineering*. New York: McGraw–Hill, 543 p.

Hartogensis, O. K., H. A. R. De Bruin, and B. J. H. Van de Wiel (2002) Displaced-beam small aperture scintillometer test. Part II: CASES-99 stable boundary-layer experiment. *Boundary-Layer Meteorology*, **105**, 149–176.

Haugen, D. A., J. C. Kaimal, and E. F. Bradley (1971) An experimental study of Reynolds stress and heat flux in the atmospheric surface layer. *Quarterly Journal of the Royal Meteorological Society*, **97**, 168–180.

Hill, R. J. (1997) Algorithms for obtaining atmospheric surface-layer fluxes from scintillation measurements. *Journal of Atmospheric and Oceanic Technology*, **14**, 456–467.

_____, **and S. F. Clifford** (1978) Modified spectrum of atmospheric temperature fluctuations and its application to optical propagation. *Journal of the Optical Society of America*, **68**, 892–899.

_____, **and R. G. Frehlich** (1997) Probability distribution of irradiance for the onset of strong scintillation. *Journal of the Optical Society of America A.*, **14**, 1530–1540.

____, R. A. Bohlander, S. F. Clifford, R. W. McMillan, J. T. Priestley, and W. P. Schoenfeld (1988) Turbulence-induced millimeter-wave scintillation compared with micrometeorological measurements. *IEEE Transactions on Geoscience and Remote Sensing*, **26**, 330–342.

____, G. R. Ochs, and J. J. Wilson (1992a) Measuring surface-layer fluxes of heat and momentum using optical scintillation. *Boundary-Layer Meteorology*, **58**, 391–408.

____, ____, and ____ (1992b) Surface-layer fluxes measured using the C_T^2-profile method. *Journal of Atmospheric and Oceanic Technology*, **9**, 526–537.

Högström, U. (1988) Non-dimensional wind and temperature profiles in the atmospheric surface layer: A re-evaluation. *Boundary-Layer Meteorology*, **42**, 55–78.

Holtslag, A. A. M., and H. A. R. De Bruin (1988) Applied modeling of the nighttime surface energy balance over land. *Journal of Applied Meteorology*, **27**, 689–704.

Horst, T. W., and J. C. Weil (1992) Footprint estimation for scalar flux measurements in the atmospheric surface layer. *Boundary-Layer Meteorology*, **59**, 279–296.

____, and ____ (1994) How far is far enough?: The fetch requirements for micrometeorological measurement of surface fluxes. *Journal of Atmospheric and Oceanic Technology*, **11**, 1018–1025.

Jordan, R. E., E. L Andreas, and A. P. Makshtas (1999) Heat budget of snow-covered sea ice at North Pole 4. *Journal of Geophysical Research*, **104**, 7785–7806.

Kiehl, J. T., and K. E. Trenberth (1997) Earth's annual global mean energy budget. *Bulletin of the American Meteorological Society*, **78**, 197–208.

Kohsiek, W., and M. H. A. J. Herben (1983) Evaporation derived from optical and radio-wave scintillation. *Applied Optics*, **22**, 2566–2570.

Large, W. G., and S. Pond (1982) Sensible and latent heat flux measurements over the ocean. *Journal of Physical Oceanography*, **12**, 464–482.

Lenschow, D. H., J. Mann, and L. Kristensen (1994) How long is long enough when measuring fluxes and other turbulence statistics? *Journal of Atmospheric and Oceanic Technology*, **11**, 661–673.

Lumley, J. L., and H. A. Panofsky (1964) *The Structure of Atmospheric Turbulence*. New York: Interscience, 239 p.

Mahrt, L. (1998) Flux sampling errors for aircraft and towers. *Journal of Atmospheric and Oceanic Technology*, **15**, 416–429.

Mitchell, J. F. B. (1989) The "greenhouse" effect and climate change. *Reviews of Geophysics*, **27**, 115–139.

Nieveen, J. P., and A. E. Green (1999) Measuring sensible heat flux density over pasture using the C_T^2-profile method. *Boundary-Layer Meteorology*, **91**, 23–35.

Oncley, S. P., C. A. Friehe, J. C. Larue, J. A. Businger, E. C. Itsweire, and S. S. Chang (1996) Surface-layer fluxes, profiles, and turbulence measurements over uniform terrain under near-neutral conditions. *Journal of the Atmospheric Sciences*, **53**, 1029–1044.

Perovich, D. K., and 22 others (1999) Year on ice gives climate insights. *Transactions of the American Geophysical Union*, **80**, 481–486.

Persson, P. O. G., C. W. Fairall, E. L Andreas, P. S. Guest, and D. K. Perovich (2002) Measurements near the Atmospheric Surface Flux Group tower at SHEBA: Near-surface conditions and surface energy budget. *Journal of Geophysical Research*, **107** (C10), DOI: 10.1029/2000JC000705.

Schmid, H. P., and T. R. Oke (1990) A model to estimate the source area contributing to turbulent exchange in the surface layer over patchy terrain. *Quarterly Journal of the Royal Meteorological Society*, **116**, 965–988.

Sreenivasan, K. R., A. J. Chambers, and R. A. Antonia (1978) Accuracy of moments of velocity and scalar fluctuations in the atmospheric surface layer. *Boundary-Layer Meteorology*, **14**, 341–359.

Strohbehn, J. W. (1970) The feasibility of laser experiments for measuring the permittivity spectrum of the turbulent atmosphere. *Journal of Geophysical Research*, **75**, 1067–1076.

Tatarskii, V. I. (1961) *Wave Propagation in a Turbulent Medium*. New York: Dover, 285 p.

——— (1971) *The Effects of the Turbulent Atmosphere on Wave Propagation*. Jerusalem: Israel Program for Scientific Translations, 472 p. (NTIS: TT 68-50464.)

Thiermann, V. (1992) A displaced-beam scintillometer for line-averaged measurements of surface layer turbulence. Preprints, *Tenth Symposium on Turbulence and Diffusion*, Portland, Oregon, Boston: American Meteorological Society, 244–247.

_____, and **H. Grassl** (1992) The measurement of turbulent surface-layer fluxes by use of bichromatic scintillation. *Boundary-Layer Meteorology*, **58**, 367–389.

Treviño, G., and E. L Andreas (2000) Averaging intervals for spectral analysis of nonstationary turbulence. *Boundary-Layer Meteorology*, **95**, 231–247.

Uttal, T., and 27 others (2002) Surface Heat Budget of the Arctic Ocean. *Bulletin of the American Meteorological Society*, **83**, 255–275.

Wesely, M. L. (1976) The combined effect of temperature and humidity fluctuations on refractive index. *Journal of Applied Meteorology*, **15**, 43–49.

_____, and **E. C. Alcarez** (1973) Diurnal cycles of the refractive index structure function coefficient. *Journal of Geophysical Research*, **78**, 6224–6232.

Wyngaard, J. C. (1973) On surface-layer turbulence. *Workshop on Micro-meteorology*, D. A. Haugen, Ed., Boston: American Meteorological Society, 101–149.

_____, and **S. F. Clifford** (1978) Estimating momentum, heat and moisture fluxes from structure parameters. *Journal of the Atmospheric Sciences*, **35**, 1204–1211.

_____, and **O. R. Coté** (1971) The budgets of turbulent kinetic energy and temperature variance in the atmospheric surface layer. *Journal of the Atmospheric Sciences*, **28**, 190–201.

REPORT DOCUMENTATION PAGE

1. REPORT DATE (DD-MM-YY) December 2003	2. REPORT TYPE Technical Report	3. DATES COVERED (From - To)

4. TITLE AND SUBTITLE

Probability Distributions for the Refractive Index Structure Parameter and the Inner Scale of Turbulence and Their Implications for Flux Averaging

5a. CONTRACT NUMBER

5b. GRANT NUMBER

5c. PROGRAM ELEMENT NUMBER

6. AUTHOR(S)

Edgar L Andreas, Christopher W. Fairall, P. Ola G. Persson, and Peter S. Guest

5d. PROJECT NUMBER

5e. TASK NUMBER

5f. WORK UNIT NUMBER

7. PERFORMING ORGANIZATION NAME(S) AND ADDRESS(ES)

U.S. Army Engineer Research and Development Center
Cold Regions Research and Engineering Laboratory
72 Lyme Road
Hanover, NH 03755-1290

8. PERFORMING ORGANIZATION REPORT

ERDC/CRREL TR-03-24

9. SPONSORING/MONITORING AGENCY NAME(S) AND ADDRESS(ES)

Office of the Chief of Engineers
Washington, DC 20314-1000

10. SPONSOR / MONITOR'S ACRONYM(S)

11. SPONSOR / MONITOR'S REPORT NUMBER(S)

12. DISTRIBUTION / AVAILABILITY STATEMENT

Approved for public release; distribution is unlimited.

Available from NTIS, Springfield, Virginia 22161.

13. SUPPLEMENTARY NOTES

14. ABSTRACT

Defining the averaging time required for measuring meaningful turbulence statistics is a central problem in boundary-layer meteorology. Path-averaging scintillation instruments are presumed to confer some time-averaging benefits when the objective is to measure surface fluxes, but that hypothesis has not been tested definitively. This study uses scintillometer measurements of the inner scale of turbulence (ℓ_0) and the refractive index structure parameter (C_n^2) collected during SHEBA (the experiment to study the Surface Heat Budget of the Arctic Ocean) to investigate this question of required averaging time. The first conclusion is that the beta probability distribution is useful for representing C_n^2 and ℓ_0 measurements. Consequently, beta distributions are used to set confidence limits on C_n^2 and ℓ_0 values obtained over various averaging periods. When the C_n^2 and ℓ_0 time series are stationary, a short-term average of C_n^2 or ℓ_0 can be as accurate as a long-term average. But, as with point measurements, when time series of path-averaged C_n^2 or ℓ_0 values are nonstationary, turbulent surface fluxes inferred from these C_n^2 and ℓ_0 values can be variable and uncertain—problems that path-averaging was presumed to mitigate. Since nonstationarity turns out to be a limiting condition, the last topic is quantifying the nonstationarity with a published nonstationarity ratio and also by simply counting zero-crossings in the time series.

15. SUBJECT TERMS

Arctic	Monin–Obukhov similarity theory	Scintillation	Turbulent surface fluxes
Beta probability distribution	Path averaging	SHEBA	
Inner scale of turbulence	Refractive index structure parameter	Time averaging	

16. SECURITY CLASSIFICATION OF:

a. REPORT	b. ABSTRACT	c. THIS PAGE	17. LIMITATION OF ABSTRACT	18. NUMBER OF PAGES	19a. NAME OF RESPONSIBLE PERSON
U	U	U	U	57	19b. TELEPHONE NUMBER (include area code)

Standard Form 298 (Rev. 8-98)
Prescribed by ANSI Std. 239.18